J. Plasma Physics (1998), *vol.* 60, *part* 3, *pp.* 587–625. Printed in the United Kingdom
© 1998 Cambridge University Press

A class of driven, dissipative, energy-conserving magnetohydrodynamic equilibria with flow

MICHAEL L. GOODMAN

Computer Sciences Corporation, and Code 695, Laboratory for Extraterrestrial Physics, NASA Goddard Space Flight Center, Greenbelt, MD 20771, USA

(Received 5 January 1998)

The classical transport coefficients provide an accurate description of transport processes in collision-dominated plasmas. These transport coefficients are used in a cylindrically symmetric, electrically driven, steady-state magnetohydrodynamic (MHD) model with flow and an energy equation to study the effects of transport processes on MHD equilibria. The transport coefficients, which are functions of number density, temperature and magnetic field strength, are computed self-consistently as functions of radius R. The model has plasma-confining solutions characterized by the existence of an inner region of plasma with values of temperature, pressure and current density that are orders of magnitude larger than in the surrounding, outer region of plasma that extends outward to the boundary of the cylinder at $R = a$. The inner and outer regions are separated by a boundary layer that is an electric-dipole layer in which the relative charge separation is localized, and in which the radial electric field, temperature, pressure and axial current density vary rapidly. By analogy with laboratory fusion plasmas in confinement devices, the plasma in the inner region is confined plasma, and the plasma in the outer region is unconfined plasma. The solutions studied demonstrate that the thermoelectric current density, driven by the temperature gradient, can make the main contribution to the current density, and that the thermoelectric component of the electron heat flux, driven by an effective electric field, can make a large contribution to the total heat flux. These solutions also demonstrate that the electron pressure gradient and Hall terms in Ohm's law can make dominant contributions to the radial electric field. These results indicate that the common practice of neglecting thermoelectric effects and the Hall and electron pressure-gradient terms in Ohm's law is not always justified, and can lead to large errors. The model has three, intrinsic, universal values of β at which qualitative changes in the solutions occur. These values are universal in that they only depend on the ion charge number and the electron-to-ion mass ratio. The first such value of β (about 3.2% for a hydrogen plasma), when crossed, signals a change in sign of the radial gradient of the number density, and must be exceeded in order that a plasma-confining solution exist for a plasma with no flow. The second such value of β (about 10.4% for a hydrogen plasma), when crossed, signals a change in sign of the poloidal current density. Some of the solutions presented exhibit this current reversal. The third such value of β is about 2.67 for a hydrogen plasma. When β is greater than or equal to this value, the thermoelectric, effective electric-field-driven component of the electron heat flux cancels 50% or more of the temperature-gradient-driven ion heat flux. If appropriate boundary conditions are given on the axis $R = 0$ of the

https://doi.org/10.1017/S0022377898006928 Published online by Cambridge University Press

cylinder, the equilibrium is uniquely determined. Analytical evidence is presented that, together with earlier work, strongly suggests that if appropriate boundary conditions are enforced at the outer boundary $R = a$ then the equilibrium exhibits a bifurcation into two states, one of which exhibits plasma confinement and carries a larger axial current than the other state, which is close to global thermodynamic equilibrium, and so is not plasma-confining. Exact expressions for the two values of the axial current in the bifurcation are presented. Whether or not a bifurcation can occur is determined by the values of a critical electric field determined by the boundary conditions at $R = a$, and the constant driving electric field, which is specified. An exact expression for the critical electric field is presented. Although the ranges of the physical quantities computed by the model are a subset of those describing fusion plasmas in tokamaks, the model may be applied to any two-component, electron–ion, collision-dominated plasma for which the ion cyclotron frequency is much larger than the ion–ion Coulomb collision frequency, such as the plasma in magnetic flux tubes in the solar interior, photosphere, lower transition region, and possibly the upper transition region and lower corona.

1. Introduction

1.1. General remarks

This is the third in a series of papers that study plasma equilibria determined by the magnetohydrodynamic (MHD) model of a two-component, electron–ion plasma that includes effects of classical transport processes. The model presented here generalizes those studied in preceding papers of the series (Goodman 1992, 1993) by including thermoelectric effects and effects of flow and viscosity, and allowing for an arbitrary value of the ion charge. In all of these models the ion cyclotron frequency is assumed, and verified to be, much larger than the ion–ion collision frequency. All models assume that the equilibria are cylindrically symmetric, and depend only upon the radial coordinate R.

Classical transport coefficients (Braginskii 1965; Balescu 1988*a*) are the only known transport coefficients defined entirely in terms of local values of temperature, number density and magnetic field strength. When included in the MHD model of a plasma, they provide a complete description of the diffusive transport of energy and momentum in a collision-dominated plasma. The derivation of these transport coefficients is based on the assumptions that the plasma is close to local thermodynamic equilibrium, and that the mean free path is much smaller than the smallest length scale over which the magnetic field undergoes significant variation, so that the magnetic field may be considered locally homogeneous.

Fusion plasmas, and most space plasmas, are not collision-dominated. In these plasmas neoclassical transport (Hinton and Hazeltine 1976; Galeev and Sagdeev 1979; Hirschman and Sigmar 1981; Balescu 1988*b*) and anomalous transport (Cowley and Sudan 1997; Liewer 1984) may dominate the non-convective transport of mass, momentum and energy. However, in the MHD equilibrium model considered here the magnetic surfaces are concentric circular cylinders. For such a magnetic surface geometry, there is no neoclassical transport (Balescu 1988*b*). Anomalous transport is due to microturbulence generated by wave–particle scattering caused by resonance of particle speeds with local plasma wave phase speeds. For an electri-

https://doi.org/10.1017/S0022377898006928 Published online by Cambridge University Press

cally driven plasma, as is considered here, the transport is expected to be primarily classical provided that the component of the electric field parallel to the magnetic field ($E_\parallel \equiv \mathbf{E}\cdot\mathbf{B}/B$) is much less than the Dreicer electric field E_D (de Kluiver *et al.* 1991; Balescu 1988*b*). The Dreicer electric field is the value of the electric field above which electron runaway is expected to occur (Dreicer 1959, 1960; Parail and Pogutse 1986), and to serve as a source of free energy to drive microinstabilities leading to transport by microturbulent processes. The Dreicer field is essentially the minimum electric field necessary to accelerate an electron to the thermal speed in one collision time. In this paper anomalous transport is neglected, and in the numerical examples presented it is found that $E_\parallel/E_D \lesssim 10^{-4}$. Balescu (1988*b*) estimates that anomalous transport becomes important when $E_\parallel/E_D \gtrsim 0.21$. The relatively small values of $E_\parallel/E_D$ for the numerical examples presented here is taken to be sufficient justification for neglecting the effects of anomalous transport processes.

A study of MHD equilibria in which the transport processes are collision-dominated is important for the following reasons.

(i) The collision-dominated transport model is based on well-understood kinetic processes, and hence a study of the corresponding equilibria provides insight into the properties of steady states of collision-dominated plasmas.

(ii) A study of the properties of these equilibria may provide at least a qualitative indication of the effects of transport processes in plasmas in which the transport processes are not collision-dominated but are not as well understood or as amenable to the same high level of analysis as in the collision-dominated case.

(iii) The equilibrium solutions may be used as initial states for time-dependent MHD simulations of plasmas where collisions may or may not dominate the transport processes.

(iv) The use of transport coefficients that are in general anisotropic, and that are functions of temperature, density and magnetic field strength, which are themselves functions of position and time, is the next logical step beyond the use of *ad hoc* constant, scalar transport coefficients that is common in MHD modelling.

The calculations and results presented in this paper are somewhat involved and numerous. For this reason, it is useful to present a condensed outline of the model and the main results. This is done in Sec. 1.2.

1.2. Outline of the model and main results

1.2.1. Basic equations. The basic equations are presented in Sec. 2. They consist of the conservation equations for mass, momentum and energy, together with Ohm's law, Maxwell's equations and the ideal-gas equation of state, assuming quasineutrality. The transport coefficients are tensors. The effects of transport appear through the viscosity tensor in the momentum equation, the electrical conductivity and thermoelectric tensors in Ohm's law, and the viscosity, thermoelectric and electron and ion thermal conductivity tensors in the energy equation. The transport coefficients are functions of position, since they are functions of the local values of magnetic field strength, temperature and density. They are computed self-consistently at each point together with the magnetic field strength, temperature and density. The high-magnetic-field approximation to the transport coefficients is used, which means that for all of the solutions presented $(\omega_i\tau_i)^2 \gg 1$, where ω_i is the ion

https://doi.org/10.1017/S0022377898006928 Published online by Cambridge University Press

cyclotron frequency and τ_i is the ion–ion collision time. In addition, the Coulomb logarithm, which occurs in the expressions for the transport coefficients, is assumed to be constant and equal to its value at $R = 0$.

The only effect of viscosity is to constrain the plasma flow to be constant and parallel to the magnetic field. Once this constraint has been enforced, the viscosity terms vanish from the momentum and energy equations. This simple effect of viscosity is essentially a consequence of the model being one-dimensional, all quantities depending only on the radius R in cylindrical coordinates. This effect is independent of the high-magnetic-field approximation to the transport coefficients.

A constant, specified, driving electric field parallel to the axis of the cylinder supplies the energy necessary to maintain the plasma in a steady state away from global thermodynamic equilibrium. The energy equation in Sec. 2.6 states that the rate at which the driving electric field does work on the axial current density is equal to rate at which energy is thermally conducted out of the plasma in the radial direction. The radially inward Poynting flux of electromagnetic energy is transformed through electric-current dissipation into thermal energy, which flows radially outward.

1.2.2. Boundary conditions and input parameters. The basic equations are reduced to a set of four coupled, nonlinear, ordinary differential equations for the temperature $T(R)$, pressure $p(R)$, axial magnetic field $B_z(R)$ and poloidal magnetic field $B_\theta(R)$. In these equations the constant driving electric field E_z and the constant flow velocity $U_\parallel$ parallel to the magnetic field, are parameters that are specified. These equations are presented in Sec. 4. Their solution is uniquely determined by specifying the boundary conditions $T(0), p(0), B_z(0)$ and $U_z(0)(\equiv U_\parallel)$, specifying E_z, and enforcing the constraints that $B_\theta(0) = 0$ and that $(B_\theta(R)/R)_{R=0}$ be given by (82). This is the set of inputs used to generate the numerical solutions presented in Sec. 5.

Once the boundary conditions at $R = 0$ and the input parameters have been specified, the equations for T, p, B_z and B_θ are integrated from $R = 0$ out to a specified radius $R = a$. For the solutions presented in Sec. 5, the choice $a = 50$ cm is made, since this is a reasonable value for modelling tokamaks. The integration is simply stopped at $R = a$. No boundary conditions are enforced at $R = a$. In principle, the integration may be continued out to $R = \infty$. However, as R increases, eventually $\omega_i\tau_i$, the Coulomb logarithm and the degree of ionization as determined by the Saha equation decrease to such small values that the high-magnetic-field approximation to the transport coefficients, the assumption that the Coulomb logarithm is constant and the assumption of complete ionization become invalid. For a given value of radius a, inputs are chosen that yield a solution that satisfies these three assumptions.

The boundary values and input parameter values used in Sec. 5 characterize tokamak plasmas of fusion interest, although the model is valid for a much wider range of these values. Radial profiles of temperature, pressure, number density, radial electric field, and the axial and poloidal components of the magnetic field, flow velocity and current density are generated for each equilibrium. These profiles appear to be reasonable, and may provide insight into the properties of tokamak plasma equilibria.

1.2.3. Plasma-confining solutions. The basic idea of generating fusion energy under laboratory conditions is to use magnetic forces to compress a plasma to sufficiently

https://doi.org/10.1017/S0022377898006928 Published online by Cambridge University Press

high temperatures and densities that nuclear fusion occurs. The plasma in such a state of compression is confined to the interior of a containment device such as a tokamak, and is separated from the wall of the device by plasma with a much lower temperature and heating rate. Such a compressed plasma is called a confined plasma. In the ideal case, the temperature, pressure and current density of a confined plasma are orders of magnitude larger than those of the surrounding plasma that comes into contact with the wall of the containment vessel. The plasma in the vessel may be viewed as being separated into an inner region of confined plasma and a contiguous, surrounding outer region of unconfined plasma that extends to the wall of the containment vessel.

Some of the solutions presented in Sec. 5 have properties similar to those of a confined plasma, and are called plasma-confining solutions. Consistent with the above definition of a confined plasma, these solutions are identified by the clear separation of the plasma into an inner region and an outer region such that the inner region has values of temperature, pressure, and axial and poloidal current densities that are one or more orders of magnitude larger than in the surrounding outer region. Practically all of the heating, which in this model is due to current dissipation, takes place in the inner region. The outer region of plasma extends to the artificial boundary at $R = a$. The boundary is artificial, since, as discussed in Sec. 1.2.2, the solutions in Sec. 5 are generated without enforcing any boundary conditions at $R = a$. In a more realistic model, some boundary conditions would be enforced at $R = a$, such as specifying the rate of plasma loss at the wall of the containment vessel, no-slip boundary conditions, stress-free boundary conditions, and boundary conditions on the electric field that depend on the dielectric properties of the wall material.

In Goodman (1993), and in the model presented here, the inner and outer regions of plasma-confining solutions are found to be separated by a boundary layer that is an electric-dipole layer in which the relative charge separation is localized, and in which the temperature, pressure, radial electric field and axial current density vary rapidly.

1.2.4. Bifurcation of the equilibrium state. Although the solutions presented in this paper are generated by specifying boundary conditions only at $R = 0$, it is claimed that any solution to the model can be generated by specifying appropriate boundary conditions at $R = a$, and then integrating from $R = a$ to $R = 0$. It is also claimed that, for certain choices of the set of values $\Psi(a) \equiv (T(a), p(a), B_z(a), T'(a), B'_z(a))$ and of E_z, where the prime denotes differentiation with respect to R, there are exactly two solutions having different values of the total axial current I_z calculated from the double-valued expression (73). If the set of boundary values $\Psi(a)$ is given and held fixed while E_z is varied, the number of solutions varies from zero to two. Only when E_z exceeds a critical value E_{crit}, defined analytically in Sec. 3.6, and determined by $\Psi(a)$, are there two allowed solutions, suggesting a bifurcation of the equilibrium state similar to that found in earlier models (Goodman 1992, 1993). For each solution presented in Sec. 5, generated by specifying only boundary conditions at $R = 0$, the corresponding values of $\Psi(a)$ and E_z are substituted into (73) to compute the two corresponding values of I_z. One of these values must be, and is found to be, equal to I_z for the solution from which $\Psi(a)$ is originally obtained. The other value of I_z, when real and positive, is claimed to correspond to another solution having the same value of $\Psi(a)$. Although numerical examples of this second

https://doi.org/10.1017/S0022377898006928 Published online by Cambridge University Press

state are not yet available for the model presented here, it is claimed that they exist. These two solutions with the same value of $\Psi(a)$ represent a bifurcation of the equilibrium state that occurs when the driving electric field exceeds $E_{\rm crit}$.

The determination of the boundary conditions at $R = a$ that uniquely determine the solution to the model, and the generation of both states in the bifurcation from these boundary conditions, is a task for the future. The same task is carried out for the models presented in Goodman (1992, 1993), and the results are now briefly reviewed.

For the simpler model presented in Goodman (1993), a double-valued expression for I_z is derived, and it is shown that specifying $T(a), p^*(a), B_z(a)$, $B'_z(a)$ and E_z uniquely determines the solution, where $p^* \equiv p + B^2/8\pi$ is the total pressure. The model exhibits a bifurcation in the following sense. The double-valued expression for I_z contains an analytical expression for a critical electric field $E_{\rm crit}$ completely determined by the ratio $B'_z(a)/T^{3/2}(a)$. If $E_z < E_{\rm crit}$, there are no real solutions for I_z. If $E_z = E_{\rm crit}$, there is one real solution for I_z, and if $E_z > E_{\rm crit}$, there are two real solutions for I_z. In the last case it is found numerically that if $B_z(a), p^*(a)$ and $E_{\rm crit}$ are given, there are exactly two values of $T(a)$, or equivalently of $B'_z(a)$ since $E_{\rm crit}$ is given, corresponding to two solutions with the two different values of I_z. As the value of E_z crosses $E_{\rm crit}$ from below, the number of solutions with the same values of $B_z(a), p^*(a)$ and $E_{\rm crit}$ jumps from zero to two. When two such solutions exist it is found that one solution is a plasma-confining solution as defined in Sec. 1.2.3, while the other solution has nearly constant values of p, T, B_z, n and j_z, where n and j_z are the number density and axial current density. The latter solution clearly does not exhibit plasma confinement, and for the numerical example presented it is found that I_z for this solution is about 452 times smaller than for the corresponding plasma-confining solution.

For the even simpler model presented in Goodman (1992), it is shown that specifying $p(a), T(a), p'(a)$, the assumed constant axial magnetic field B_z, and E_z uniquely determines the solution. The model exhibits a bifurcation in the following sense. When $p(a)$, $T(a)$, and B_z are given, it is shown numerically that if E_z is *less than* a critical value $E_{\rm crit}$, two solutions exist. One solution is a plasma-confining solution as defined in Sec. 1.2.3, while the other solution has nearly constant values of p, T, n and j_z. The latter solution clearly does not exhibit plasma confinement, and for the numerical example presented it is found that I_z for this solution is about 43 times smaller than for the corresponding plasma confining solution. When $E_z > E_{\rm crit}$, only the plasma-confining solution exists. Approximate analytical expressions for $E_{\rm crit}$ and I_z for the solutions that have nearly constant values of p, T, n and j_z are derived.

These bifurcations may be related to the L–H mode transition observed in tokamaks (e.g. Taylor *et al.* 1989; Zhang *et al.* 1993). Controlling the driving electric field and the properties of the plasma at its outer boundary may allow for establishing and maintaining a global state of plasma confinement. It is suggested that if the driving electric field exceeds a critical value then a bifurcation of the steady state of the plasma is possible.

The importance of dissipative processes in MHD in giving rise to a bifurcation of the equilibrium state is discussed by Spada (1992), and their importance in determining the existence and uniqueness of the equilibrium state in the case of classical transport is discussed by Spada and Wobig (1992). The models studied by Spada (1992) and Spada and Wobig (1992) and the model considered here are

https://doi.org/10.1017/S0022377898006928 Published online by Cambridge University Press

one-temperature models. Important effects are expected to arise as a result of unequal ion and electron temperatures. Classical transport effects on the existence of equilibria in a two-temperature MHD model are discussed by Hu (1982).

1.2.5. Critical, universal values of β. In Sec. 3.4.1 it is shown that the poloidal current density reverses direction when, and only when β crosses a critical value $\beta_{j,\mathrm{crit}}(Z,\mu)$ that depends only on the ion charge number Z and the ion-to-electron mass ratio μ. For a hydrogen plasma, $\beta_{j,\mathrm{crit}} \approx 10.4\%$.

In Sec. 3.4.2 it is shown that the gradient of the ion number density, n_i', changes sign when, and only when, β crosses a critical value $\beta_{n,\mathrm{crit}}(R)$. In the presence of flow $\beta_{n,\mathrm{crit}}(R)$ depends on the local state of the plasma, and hence on the boundary conditions and input parameters. In the absence of flow $\beta_{n,\mathrm{crit}}(R)$ is independent of R. In this case n_i' can reverse sign only for $Z = 1$, and this reversal occurs when β crosses the value $\beta^0_{n,\mathrm{crit}}(Z = 1, \mu)$, which is about 3.2% for a hydrogen plasma.

The values $\beta_{j,\mathrm{crit}}(Z,\mu)$ and $\beta^0_{n,\mathrm{crit}}(Z = 1, \mu)$, are universal in that they depend only on Z and μ. Therefore these values of β are the same for all solutions having the same ion charge and mass, regardless of how the solutions differ in boundary conditions, input parameters, and cylinder radius.

For plasma-confining equilibria, it is found that there is one value of $R > 0$ at which $\beta(R) = \beta_{n,\mathrm{crit}}(R)$. The number density is a minimum at this value of R, which defines the location of the boundary layer that separates the inner region of confined plasma from the outer region of unconfined plasma. This boundary layer, which is a cylindrical annulus, is a localized internal region of depleted plasma density. For plasma-confining equilibria, it is also found that if the poloidal current density changes sign, the region of negative current density is confined almost entirely to the boundary layer. In this case the boundary layer is a localized internal region of poloidal current reversal.

A third universal value of β that depends only on Z and μ, and that determines the degree to which the thermoelectric electron heat flux cancels the ion heat flux, is discussed in Sec. 1.2.6.

1.2.6. Thermoelectric effects in determining the current density and electron heat flux. It is common practice to omit thermoelectric effects in MHD modelling of plasmas. In the context of MHD with classical transport effects, thermoelectric effects enter the model through Ohm's law (23) and the electron heat flux (36) in the energy equation. Thermoelectric effects do not make any contribution to the ion heat flux (37).

The thermoelectric term in Ohm's law couples the axial and poloidal current densities to the temperature gradient through the thermoelectric tensor. Through this coupling, the radial temperature gradient drives an axial and poloidal current density. It is shown in Sec. 5 that the axial component of the thermoelectric current density can be as much as six times larger than the axial component of the familiar conduction current density, which is proportional to the conductivity tensor, and driven by the effective electric field defined by (25). It is also shown in Sec. 5 that the poloidal component of the thermoelectric current density can be as much as 10^2 times larger than the poloidal component of the conduction current density. These results prove that the temperature gradient can be the dominant mechanism of current drive through thermoelectric effects.

The thermoelectric term in the expression for the electron heat flux couples this

https://doi.org/10.1017/S0022377898006928 Published online by Cambridge University Press

flux to the effective electric field through the thermoelectric tensor. Through this coupling, the effective electric field drives an electron heat flux, which must be added to the familiar temperature-gradient-driven part of the electron heat flux. Only the radial components of the electron and ion heat flux appear in the energy equation in the model considered here. In the model the radial component of the magnetic field is zero, and the radial component of the temperature-gradient-driven ion heat flux is $(m_i/m_e)^{1/2}$ (≈ 43 for hydrogen) times the radial component of the temperature-gradient-driven part of the electron heat flux, where m_i and m_e are the electron and ion masses. This is an example of the well-known result that the ions dominate the temperature-gradient-driven heat flux across magnetic field lines in a magnetized plasma. However, it is shown in Secs 2.6 and 5.2 that the thermoelectric component of the electron heat flux is radially inward, driven by the effective electric field from lower to higher temperatures. For $\beta \geqslant 4(1 + Z)/3Z$ (≈ 2.67 for hydrogen), this component of the heat flux cancels 50% or more of the radially outward, temperature-gradient-driven ion heat flux. For some of the solutions in Sec. 5, this cancellation is as large as about 80%. These results prove that the thermoelectric component of the electron heat flux can make a large contribution to the total heat flux.

1.2.7. Electron-pressure-gradient and Hall effects in determining the electric field. Electron-pressure and Hall effects are often neglected in MHD modelling of plasmas. The Hall and electron-pressure-gradient terms occur in Ohm's law (23) in the term proportional to the electrical conductivity tensor. For the model presented here, the radial electric field is the sum of the electric fields generated by the Hall and electron-pressure-gradient terms. It is shown in Sec. 5 that the ratio of these terms can be $\gg$, $\ll$ or ≈ 1.

CGS units are used unless indicated otherwise.

2. Basic equations

In cylindrical coordinates (R, θ, z) the equilibrium depends only on the radius R. The plasma is assumed to be strongly magnetized, so the high magnetic field limit of the transport coefficients is used. The plasma is strongly magnetized if $(\omega_e\tau_e)^2 \gg 1$ and $(\omega_i\tau_i)^2 \gg 1$, where $\omega_{i,e}$ are the ion and electron cyclotron frequencies, and $\tau_{i,e}$ are the ion–ion and electron–ion collision times. It is verified for the solutions presented in Sec. 5 that the plasma is strongly magnetized. The Coulomb logarithm is assumed to be constant and equal to its value at $R = 0$, and for the solutions presented in Sec. 5 it varies by less than 50% throughout the plasma from its value at $R = 0$. The plasma is assumed to consist of electrons and one type of ion with charge number Z. For a hydrogen plasma, this assumption is equivalent to that of complete ionization, and is verified for the solutions presented in Sec. 5 by using the Saha equation (Mihalas and Mihalas 1984) to compute the degree of ionization. The general MHD equations and the expressions for the transport coefficients are taken from Balescu (1988*a*), assuming that the electron and ion temperatures are equal, which allows the electron and ion energy equations to be combined into a single equation. The model is valid for any value of the ion mass and charge.

The high-magnetic-field approximation is not made until Sec. 2.5, after the general form of Ohm's law has been presented.

https://doi.org/10.1017/S0022377898006928 Published online by Cambridge University Press

2.1. Maxwell's equations

Let $\mathbf{B}, \mathbf{E}$ and $\mathbf{j}$ be the magnetic and electric fields and the current density. Since all quantities depend only on R, Maxwell's equations reduce to $B_R = E_\theta = j_R = 0$, E_z = constant and

$$j_\theta = \frac{-cB_z'}{4\pi}, \tag{1}$$

$$j_z = \frac{c(RB_\theta)'}{4\pi R}, \tag{2}$$

where the prime denotes differentiation with respect to R.

E_z is the constant driving electric field, which provides the energy necessary to prevent the plasma from relaxing to global thermodynamic equilibrium by current dissipation. E_z is an input to the model, and (as shown in Sec. 3.6), under certain conditions, must exceed a critical value in order that an equilibrium exist.

2.2. Continuity equation

Let $\mathbf{U}$ be the flow velocity, which is essentially the ion flow velocity. Then the continuity equation $\boldsymbol{\nabla} \cdot (\rho \mathbf{U}) = 0$, where ρ is the ion mass density, reduces to the condition that $U_R = 0$.

2.3. The viscosity tensor in cylindrical coordinates

The viscosity tensor is derived and discussed in detail by Balescu (1988*a*) using a local Cartesian coordinate system with one axis aligned with the local magnetic field. For the model considered here, the viscosity tensor is transformed from this local coordinate system to the global cylindrical coordinate system. The viscosity tensor is called the dissipative pressure tensor by Balescu (1988*a*).

The viscosity tensor enters the basic equations through the momentum and energy equations. The viscosity tensor enters the momentum equation through the term $\boldsymbol{\nabla} \cdot (\boldsymbol{\Pi}^e + \boldsymbol{\Pi}^i)$, where $\boldsymbol{\Pi}^e$ and $\boldsymbol{\Pi}^i$ are the electron and ion viscosity tensors. The viscosity tensor enters the energy equation through the term $(\boldsymbol{\Pi}^e + \boldsymbol{\Pi}^i) :: \boldsymbol{\nabla}\mathbf{U}$, where :: denotes the tensor scalar product.

Carrying out the transformation from local Cartesian to global cylindrical coordinates gives

$$\Pi^a_{RR} = \eta^a_3 U'_\perp, \tag{3}$$

$$\Pi^a_{\theta\theta} = -2\eta^a_1 U'_\parallel \alpha_\theta \alpha_z - \eta^a_3 U'_\perp \alpha_z^2, \tag{4}$$

$$\Pi^a_{zz} = 2\eta^a_1 U'_\parallel \alpha_\theta \alpha_z - \eta^a_3 U'_\perp \alpha_\theta^2, \tag{5}$$

$$\Pi^a_{R\theta} = \Pi^a_{\theta R} = -\eta^a_2 U'_\parallel \alpha_\theta - \eta^a_4 U'_\perp \alpha_z, \tag{6}$$

$$\Pi^a_{Rz} = \Pi^a_{zR} = -\eta^a_2 U'_\parallel \alpha_z + \eta^a_4 U'_\perp \alpha_\theta, \tag{7}$$

$$\Pi^a_{\theta z} = \Pi^a_{z\theta} = -\eta^a_1 U'_\parallel (\alpha_z^2 - \alpha_\theta^2) + \eta^a_3 U'_\perp \alpha_\theta \alpha_z, \tag{8}$$

where $a = e, i$ for electrons or ions, the η^a_j $(j = 1, 2, 3, 4)$ are the viscosity coefficients defined by Balescu (1988*a*), α_θ and α_z are defined as

$$\alpha_\theta \equiv \frac{B_\theta}{B}, \tag{9}$$

$$\alpha_z \equiv \frac{B_z}{B}, \tag{10}$$

https://doi.org/10.1017/S0022377898006928 Published online by Cambridge University Press

and $U_\perp$ and $U_\parallel$ are the components of $\mathbf{U}$ perpendicular and parallel to $\mathbf{B}$, and are computed from the relations

$$U_\perp = U_\theta \alpha_z - U_z \alpha_\theta, \tag{11}$$

$$U_\parallel = U_\theta \alpha_\theta + U_z \alpha_z. \tag{12}$$

The explicit forms of the viscosity coefficients are not needed here. It is only necessary to know that η_1 and η_3 are zero at a point if and only if $B = 0$ at that point. For the equilibria considered here, $B \neq 0$.

The terms in the momentum and energy equations involving the viscosity tensor may then be computed from the equations

$$\boldsymbol{\nabla} \cdot \boldsymbol{\Pi}^a = \frac{(R\Pi^a_{RR})' - \Pi^a_{\theta\theta}}{R} \hat{\mathbf{R}} + \left(\Pi^a_{R\theta}{}' + \frac{2\Pi^a_{R\theta}}{R} \right) \hat{\theta} + \frac{(R\Pi^a_{Rz})'}{R} \hat{\mathbf{z}} \tag{13}$$

and

$$\boldsymbol{\Pi}^a :: \boldsymbol{\nabla}\mathbf{U} = R\Pi^a_{R\theta} \left(\frac{U_\theta}{R} \right)' + \Pi^a_{Rz} U_z', \tag{14}$$

where $\hat{\mathbf{R}}$, $\hat{\theta}$ and $\hat{\mathbf{z}}$ are unit vectors in the R, θ and z directions.

2.4. Momentum equation

The general form of the momentum equation is

$$\rho \mathbf{U} \cdot \boldsymbol{\nabla}\mathbf{U} + \boldsymbol{\nabla} p = \frac{\mathbf{j} \times \mathbf{B}}{c} - \boldsymbol{\nabla} \cdot (\boldsymbol{\Pi}^e + \boldsymbol{\Pi}^i), \tag{15}$$

where p and c are the total fluid pressure and speed of light. Here $p = p_e + p_i$, where p_e and p_i are the electron and ion pressures.

Require that the elements of the viscosity tensor be finite at $R = 0$. Then the θ and z components of the momentum equation reduce to

$$\Pi^e_{R\theta} + \Pi^i_{R\theta} = 0, \tag{16}$$

$$\Pi^e_{Rz} + \Pi^i_{Rz} = 0, \tag{17}$$

which, according to (6) and (7), may be written as

$$(\eta^e_2 + \eta^i_2)\alpha_\theta U_\parallel' + (\eta^e_4 + \eta^i_4)\alpha_z U_\perp' = 0, \tag{18}$$

$$(\eta^e_2 + \eta^i_2)\alpha_z U_\parallel' - (\eta^e_4 + \eta^i_4)\alpha_\theta U_\perp' = 0. \tag{19}$$

Since $B \neq 0$, the only solution to (18) and (19) is $U_\parallel(R) = c_1$ and $U_\perp(R) = c_2$, where c_1 and c_2 are constants. At $R = 0$, one has $U_\theta = B_\theta = 0$, so it follows from (11) and (12) that

$$U_\perp(R) = 0, \tag{20}$$

$$U_\parallel(R) = U_z(0). \tag{21}$$

Hence the flow is constrained to be everywhere parallel to the magnetic field, with a magnitude equal to the flow speed along the axis of the cylinder at $R = 0$. This result is independent of the high-magnetic-field approximation, and is essentially a consequence of the assumption that the equilibrium state is only a function of R. Any flow orthogonal to the magnetic field induces viscous stresses that cannot be balanced by inertial, pressure or Lorentz forces. The axial flow velocity $U_z(0)$ is an input to the model. Equilibria with no flow may be generated by setting $U_z(0) = 0$.

https://doi.org/10.1017/S0022377898006928 Published online by Cambridge University Press

The remaining, radial component of the momentum equation may now be written as

$$-\rho\frac{U_\theta^2}{R}+p'=\frac{j_\theta B_z-j_z B_\theta}{c}. \tag{22}$$

2.5. Ohm's law

The general form of Ohm's law is

$$\mathbf{j}=\boldsymbol{\sigma}\cdot\left(\mathbf{E}+\frac{\mathbf{U}\times\mathbf{B}}{c}+\frac{\boldsymbol{\nabla}p_e}{en_e}\right)-\boldsymbol{\alpha}\cdot\boldsymbol{\nabla}T \tag{23}$$

$$\equiv\mathbf{j}_{\rm cond}+\mathbf{j}_{te}. \tag{24}$$

Here n_e is the electron number density, and $\mathbf{j}_{\rm cond}$ and $\mathbf{j}_{te}$ are the conduction and thermoelectric current densities driven by the effective electric field

$$\mathbf{E}_{\rm effective}\equiv\mathbf{E}+\frac{\mathbf{U}\times\mathbf{B}}{c}+\frac{\boldsymbol{\nabla}p_e}{en_e}, \tag{25}$$

and the temperature gradient respectively. $\boldsymbol{\sigma}$ is the electrical conductivity tensor, with components $\sigma_\parallel,\sigma_\perp$ and $\sigma_\wedge$, which are the parallel, perpendicular and Hall conductivities. $\boldsymbol{\alpha}$ is the thermoelectric tensor, with components $\alpha_\parallel,\alpha_\perp$ and $\alpha_\wedge$, which are the parallel, perpendicular and Hall thermoelectric coefficients. The parallel and perpendicular directions are defined with respect to the local magnetic field. The notation for the components of the electrical conductivity, thermal conductivity (introduced in Sec. 2.6) and thermoelectric tensors is the same as in Balescu (1988*a*). e is the magnitude of the electron charge. In Balescu (1988*a*), Boltzmann's constant is defined as unity, and ω_e is defined as negative although e is positive. Here $\omega_e>0$, but, following Balescu, Boltzmann's constant is set equal to unity, so the dimension of temperature T in all formulas is that of energy (ergs).

At this point, the high-magnetic-field approximation is made. This means that in the remainder of the paper all equations are valid only through leading order in $\omega_i\tau_i$ and $\omega_e\tau_e$. In this approximation, the three components of Ohm's law reduce to the following expressions for the poloidal and axial current densities and the radial electric field.

The poloidal current density is given by

$$j_\theta=-\frac{cB_z{}'}{4\pi}=\left(\sigma_\parallel-\frac{\sigma_\wedge^2}{\sigma_\perp}\right)\alpha_\theta\alpha_z E_z+\frac{\sigma_\wedge\alpha_\perp}{\sigma_\perp}\alpha_z T' \tag{26}$$

$$=\alpha_z\left[\sigma_\parallel\left(1-\frac{1}{\Sigma_\parallel}\right)\alpha_\theta E_z+\omega_e\tau_e\alpha_\perp T'\right]. \tag{27}$$

The axial current density is given by

$$j_z=\frac{c\,(RB_\theta)'}{4\pi R}=\left(\sigma_\parallel\alpha_z^2+\frac{\sigma_\wedge^2}{\sigma_\perp}\alpha_\theta^2\right)E_z-\frac{\sigma_\wedge\alpha_\perp}{\sigma_\perp}\alpha_\theta T' \tag{28}$$

$$=\sigma_\parallel\left(\alpha_z^2+\frac{\alpha_\theta^2}{\Sigma_\parallel}\right)E_z-\omega_e\tau_e\alpha_\perp\alpha_\theta T'. \tag{29}$$

The radial electric field is given by

$$E_R=\frac{1}{\sigma_\perp}\left[\alpha_\perp T'-\frac{\sigma_\perp}{en_e}(n_eT)'-\sigma_\wedge\alpha_\theta E_z\right] \tag{30}$$

https://doi.org/10.1017/S0022377898006928 Published online by Cambridge University Press

$$= -\omega_e \tau_e \alpha_\theta E_z \left\{ \frac{3(2\mu)^{1/2}}{2\beta\delta} \left[1 + \frac{3Z\beta}{4\,(1+Z)} \right] + 1 \right\} - \frac{m_i U_\theta^2}{e\,(1+Z)\,R} \tag{31}$$

$$= \frac{1}{eZn_i} \left[\frac{(\mathbf{j} \times \mathbf{B})_R}{c} - p_e' \right], \tag{32}$$

where

$$\delta = 1 + \mu^{1/2} \left(1 + \frac{Z}{2^{1/2}} \right) \approx 1, \tag{33}$$

$\mu = m_e/m_i$, m_e and m_i are the electron and ion masses, Z is the ion charge number, and $\beta = p/(B^2/8\pi)$. Since, as shown in Sec. 3.1, $B_\theta E_z \geqslant 0$, it follows from (31) that $E_R \leqslant 0$.

Equations (27), (29), (31) and (32) are obtained from (26), (28) and (30) by using the expressions for the transport coefficients in Sec. 2.7.

Three equivalent expressions (30)–(32) are given for the radial electric field. Equation (32) is identical to the radial component of the electric field derived using the ideal MHD Ohm's law including the Hall and electron-pressure-gradient terms, so that thermoelectric and resistive effects do not appear explicitly in E_R. The variation of E_R with R implies a non-zero charge separation, discussed in more detail in Secs. 3.3 and 5, which, although small compared with the electron charge density, consistent with the replacement of Coulomb's law by the quasineutrality condition in the MHD approximation, can lead to the formation of an internal electric-dipole layer in the plasma. Examples of these dipole layers appear in the solutions discussed in Sec. 5.

2.6. Energy equation

The electrons and ions are assumed to have the same temperature T. The quasineutrality condition $n_e = Zn_i$ is assumed to hold, where n_i is the ion number density.

The energy equation may be written as

$$\frac{c}{4\pi} E_z B_\theta = -\left(\kappa_\perp^e + \kappa_\perp^i - \frac{\alpha_\perp^2}{\sigma_\perp} T \right) T' - \frac{\alpha_\perp \sigma_\wedge}{\sigma_\perp} \alpha_\theta T E_z, \tag{34}$$

which, after using the expressions for the transport coefficients in Sec. 2.7, becomes

$$\frac{c}{4\pi} E_z B_\theta = -\kappa_\perp^i T' \frac{1 + \mu^{1/2}(1 + 2^{-1/2} Z)}{1 + \frac{3}{4} \frac{Z}{1+Z} \beta}. \tag{35}$$

Equation (35) states that the negative of the radial component of the Poynting flux equals the ion thermal energy flux times a factor that depends on the electron-to-ion mass ratio, the ion charge number and β. This factor includes the effects of electron electrical and thermal conduction, and thermoelectric effects. The term proportional to β comes from the term proportional to $\alpha_\perp$ in (34), and represents the major contribution of the thermoelectric component of the electron heat flux to the total heat flux. This is the contribution that does not vanish in the limit of zero electron mass (i.e. $\mu^{1/2} \to 0$). As discussed in Sec. 3.1, $B_\theta E_z \geqslant 0$. It then follows from (35) that $T' \leqslant 0$. Then the last two terms on the right-hand side of (34) show that the thermoelectric component of the heat flux is radially *inward*, which is in the direction opposite to that of the component of the electron and ion heat flux proportional to the thermal conductivities $\kappa_\perp^e$ and $\kappa_\perp^i$. The thermoelectric component of the heat flux flows from lower to higher temperatures. The thermo-

https://doi.org/10.1017/S0022377898006928 Published online by Cambridge University Press

electric heat flux is important when $\beta \gtrsim 4(1+Z)/3Z$, which is 2.67 for hydrogen, 2.0 for helium, and about 1.3 for high Z. When β reaches or exceeds these values, the contribution of the radially inward thermoelectric heat flux is significant. The term proportional to $\mu^{1/2}$ represents the contribution of the component of the electron heat flux proportional to the thermal conductivity $\kappa_\perp^e$ and the contribution of those thermoelectric effects that vanish in the limit of zero electron mass. This term is small compared with unity, and so makes little contribution to the transport of thermal energy across the magnetic field. The exact expressions for the electron and ion heat fluxes are given by Balescu (1988*a*) as

$$\mathbf{q}^e = T_e \boldsymbol{\alpha} \cdot \mathbf{E}_{\text{effective}} - \boldsymbol{\kappa}^e \cdot \boldsymbol{\nabla} T_e \tag{36}$$

and

$$\mathbf{q}^i = -\boldsymbol{\kappa}^i \cdot \boldsymbol{\nabla} T_i, \tag{37}$$

where $\boldsymbol{\kappa}^e$ and $\boldsymbol{\kappa}^i$ are the electron and ion thermal conductivity tensors, and T_e and T_i are the electron and ion temperatures. Equation (36) shows that the effective electric field, defined by (25), drives the thermoelectric contribution to the electron heat flux.

Since $T' < 0$ for $R > 0$, the total heat flux is always radially outward. The radially outward, temperature-gradient-driven, ion heat flux always exceeds the radially inward, effective electric-field-driven, thermoelectric electron heat flux, although substantial cancellation may occur between the two fluxes as shown in Sec. 5.

Viscosity does not enter the energy equation (34) for the following reason. The exact energy equation involves the viscosity tensors only in a term proportional to $(\boldsymbol{\Pi}^e + \boldsymbol{\Pi}^i) :: \boldsymbol{\nabla}\mathbf{U}$. It follows from (14), (16) and (17) that

$$(\boldsymbol{\Pi}^e + \boldsymbol{\Pi}^i) :: \boldsymbol{\nabla}\mathbf{U} = 0. \tag{38}$$

The result (38) is independent of the high-magnetic-field approximation, and follows from the assumption that the equilibrium depends only on R. The only effect of viscosity in the one-dimensional model considered here is to constrain the flow velocity to be parallel to the magnetic field, and to have a constant magnitude. In a steady state, viscous dissipation and viscous transport of momentum may only occur in a higher-dimensional model that involves at least one of the coordinates θ and z, in addition to R.

2.7. Transport coefficients in the high-magnetic-field approximation

In this section explicit forms are given for the transport coefficients in (26)–(35). These coefficients depend on temperature, number density and magnetic field magnitude, which are solved for self-consistently as functions of R. Hence the transport coefficients are solved for self-consistently, so that the model self-consistently takes into account effects due to the inhomogeneity and anisotropy of the thermoelectric and thermal and electrical conductivity tensors.

The transport coefficients in Secs. 2.7.1–2.7.4 are derived from first principles, and discussed in detail, by Balescu (1988*a*).

2.7.1. Electron perpendicular thermal conductivity. This is

$$\kappa_\perp^e = \frac{1.3 + 0.5657 Z^{-1}}{(\omega_e \tau_e)^2} \frac{2.5 n_e T \tau_e}{m_e}. \tag{39}$$

https://doi.org/10.1017/S0022377898006928 Published online by Cambridge University Press

2.7.2. Ion perpendicular thermal conductivity. This is

$$\kappa_{\perp}^{i} = \frac{0.5657}{(\omega_i \tau_i)^2} \frac{2.5 n_i T \tau_i}{m_i}, \tag{40}$$

where the ion–ion collision time is given by

$$\tau_i = \frac{3}{4(2\pi)^{1/2}} \frac{{m_i}^{1/2} T^{3/2}}{Z^4 e^4 n_i \Lambda}, \tag{41}$$

and where

$$\Lambda = \ln\left(\frac{3T^{3/2}}{2e^3 \pi^{1/2} Z^{3/2} n_i^{1/2}} \right) \tag{42}$$

is the Coulomb logarithm, assumed to be constant, and set equal to its value at $R = 0$.

2.7.3. Electron parallel, perpendicular and Hall electrical conductivities. These are

$$\sigma_{\parallel} = \frac{e^2 n_e \tau_e}{m_e} \Sigma_{\parallel}, \tag{43}$$

$$\sigma_{\perp} = \frac{1}{(\omega_e \tau_e)^2} \frac{\sigma_{\parallel}}{\Sigma_{\parallel}}, \tag{44}$$

$$\sigma_{\wedge} = \frac{1}{\omega_e \tau_e} \frac{\sigma_{\parallel}}{\Sigma_{\parallel}}, \tag{45}$$

where

$$\Sigma_{\parallel} = \frac{0.31 + 1.22 Z^{-1} + 0.411 Z^{-2}}{0.091 + 0.493 Z^{-1} + 0.411 Z^{-2}}, \tag{46}$$

and where the electron–ion collision time is given by

$$\tau_e = Z^2 \mu^{1/2} \tau_i. \tag{47}$$

2.7.4. Electron perpendicular thermoelectric coefficient. This is

$$\alpha_{\perp} = \frac{0.9487(2.5)^{1/2}}{e(\omega_e \tau_e)^2} \frac{\sigma_{\parallel}}{\Sigma_{\parallel}}. \tag{48}$$

2.8. Equation of state

The electrons and ions are assumed to obey ideal gas equations of state. Then

$$p_i = n_i T, \tag{49}$$

$$p_e = Z n_i T, \tag{50}$$

$$p = (1 + Z) n_i T. \tag{51}$$

3. Exact properties of the equilibria

Only equilibria with $B \neq 0$ are considered, as required by the high-magnetic-field approximation.

https://doi.org/10.1017/S0022377898006928 Published online by Cambridge University Press

3.1. Signs of the Poynting flux and magnetic field components

It is now shown that for any solution consistent with the high-magnetic-field approximation, the Poynting flux is radially inward, and B_z and B_θ do not change sign, so there is no magnetic field reversal.

Forming the expression $\mathbf{j} \cdot \mathbf{B}$ first using (1) and (2), then using (27) and (29), and equating the two expressions gives

$$B_\theta = \frac{4\pi \Sigma_0(Z) E_z B_z(R)}{cR} \int_0^R \frac{x T^{3/2}}{B_z}\, dx, \tag{52}$$

where

$$\Sigma_0(Z) = \frac{3\Sigma_\parallel(Z)}{4Ze^2\Lambda\,(2\pi m_e)^{1/2}}. \tag{53}$$

Equation (52) shows that near $R = 0$ one has $E_z B_\theta > 0$. If $E_z B_\theta$ changes sign then $B_\theta(R^*) = 0$ for some $R^* > 0$. Then either $B_z(R^*) = 0$ or the integral in (52) is zero. If $B_z(R^*) = 0$ then $B(R^*) = 0$, in which case the high-magnetic-field assumption is violated. If the integral in (52) vanishes at $R = R^*$ then $B_z(R_1) = 0$ for at least one R_1 such that $0 < R_1 < R^*$. Choose the smallest such R_1. Assume that B_z is an analytic function of R. Then $B_z(R) \approx (R - R_1)^n$ for R near R_1, where $n \geqslant 1$ is an integer. Since B_z is analytic, its zeros are isolated. It follows that $\lim_{R \to R_1} B_\theta = 0$, which again implies that $B(R_1) = 0$, in violation of the high-magnetic-field approximation.

Therefore, for any acceptable solution, B_θ and B_z do not change sign, and $E_z B_\theta \geqslant 0$, where equality holds only at $R = 0$. These conditions hold for the solutions discussed in Sec. 5.

The radial, and only non-zero, component of the Poynting flux is $-cE_z B_\theta/4\pi$, which is zero or negative.

3.2. Sign of the Lorentz force

It follows from (27), (29) and (48) that

$$(\mathbf{j} \times \mathbf{B})_R = -\frac{\sigma_\parallel}{\Sigma_\parallel} B_\theta E_z + \frac{3ZcpT'}{2\,(1+Z)\,T} < 0, \tag{54}$$

so the Lorentz force on the plasma is always compressive. Although the magnetic pressure does not always decrease with increasing R, in the cases in which it does so the radially inward magnetic tension force $-B_\theta^2/4\pi R$ always exceeds the radially outward magnetic pressure force $-B^{2'}/8\pi$.

3.3. Relative charge separation at $R = 0$

It is a basic approximation of MHD that the relative charge separation is always small. This approximation allows Coulomb's law to be replaced by the quasineutrality condition (Freidberg 1982). The validity of this approximation is checked in the present model by the numerical evaluation of an exact expression for the relative charge separation. Some insight into the physical origin of the charge separation is

https://doi.org/10.1017/S0022377898006928 Published online by Cambridge University Press

obtained by calculating its value at $R = 0$, which is given by

$$\frac{\boldsymbol{\nabla}\cdot\mathbf{E}}{4\pi e n_e} = -\frac{Z}{1+Z}\left[\frac{U_z(0)-V_z(0)}{c}\right]^2\left\{\frac{1}{Z\Sigma_\parallel}\left[1+3\left(\frac{\mu}{2}\right)^{1/2}\frac{1+Z}{\delta}\left(\frac{1}{\beta(0)}+\frac{3}{4}\frac{Z}{1+Z}\right)\right]\right.$$
$$\left.+\frac{1}{2}\left[\frac{U_z(0)}{V_A(0)}\right]^2\right\}\leqslant 0, \tag{55}$$

where δ is given by (33), $V_z(0)$ is the z component of the electron flow speed at $R = 0$, and $V_A(0)$ is the Alfvén speed at $R = 0$. Equation (55) shows that the relative charge separation is a second-order relativistic effect, which is also the case for the model presented in Goodman (1993). As shown in Sec. 5, although the radial electric field may be as large as $10^4\ \mathrm{V\,m^{-1}}$, the relative charge separation never exceeds a value of order 10^{-7}, with the charge separation mostly confined to an internal electric-dipole layer several centimetres thick, inside of which the electric field reaches its maximum magnitude.

3.4. Critical, universal values of β

The critical values of β presented in this section signal changes in sign of the poloidal current density and the radial derivative of the number density. The value of β at which n_i' reverses sign in the absence of flow and the value of β at which j_θ reverses sign are universal in that they depend only on Z and μ.

3.4.1. Change in sign of the poloidal current density. The poloidal current density j_θ changes sign when β passes through a critical value $\beta_{j,\mathrm{crit}}$. This is seen by writing j_θ in the form

$$j_\theta = \frac{1.5\alpha_\theta\alpha_z n_e c^2 E_z}{4\pi\delta\kappa_\perp^i}\left(\frac{\beta}{\beta_{j,\mathrm{crit}}}-1\right), \tag{56}$$

where

$$\beta_{j,\mathrm{crit}}(Z,\mu)\equiv\frac{2(1+Z)}{\frac{2^{3/2}}{3}(\Sigma_\parallel-1)\left(1+\frac{Z}{2^{1/2}}+\frac{1}{\mu^{1/2}}\right)-\frac{3Z}{2}}. \tag{57}$$

For $Z = 1$ and $m_i = m_p$,

$$\beta_{j,\mathrm{crit}} = 0.104. \tag{58}$$

Examples of a reversal in j_θ are discussed in Sec. 5. j_θ reverses sign in four of the six solutions discussed. Three of these four solutions divide the plasma into an inner region where $j_\theta > 0$ and an outer region where $j_\theta < 0$. The fourth solution exhibits an annulus in the interior of the plasma in which $j_\theta < 0$, and which is surrounded by plasma in which $j_\theta > 0$.

3.4.2. Change in sign of the gradient of the number density. The radial derivative of the ion number density may be written as

$$n_i' = -\frac{n_i c E_z B_\theta Z}{4\pi{\kappa_\perp}^i T(2\mu)^{1/2}(1+Z)^2}\left\{\beta-\beta_{n,\mathrm{crit}}^0\left[2-Z\right.\right.$$
$$\left.\left.+4\delta\left(\frac{cE_zB_\theta}{4\pi}\right)^{-1}\frac{{\kappa_\perp}^i T}{R}\frac{m_i{U_\theta}^2}{2T}\right]\right\}\left[1+\frac{3(Z-2)(2\mu)^{1/2}}{8\delta}\right] \tag{59}$$
$$\equiv -\frac{n_i c E_z B_\theta Z}{4\pi\kappa_\perp^i T(2\mu)^{1/2}(1+Z)^2}[\beta-\beta_{n,\mathrm{crit}}(R)]\left[1+\frac{3(Z-2)(2\mu)^{1/2}}{8\delta}\right], \tag{60}$$

https://doi.org/10.1017/S0022377898006928 Published online by Cambridge University Press

where the last factor in (59) is of order 1, and

$$\beta^0_{n,\mathrm{crit}}(Z,\mu) \equiv \frac{(2\mu)^{1/2}(1+Z)}{2Z\delta}\left[1+\frac{3(Z-2)(2\mu)^{1/2}}{8\delta}\right]^{-1}. \tag{61}$$

For $Z = 1$ and $m_i = m_p$,

$$\beta^0_{n,\mathrm{crit}} = 0.032. \tag{62}$$

If the plasma rotates sufficiently fast then (59) shows that the number density increases with increasing R. This is found to be the case numerically in that when $U_z(0)$ is increased with all other input parameters held fixed, the poloidal flow velocity U_θ increases, and eventually becomes large enough to make $n_i'(R) > 0$. This is expected, since increasing U_θ increases the centrifugal force on the plasma.

If there is no flow, n_i' can reverse sign only for $Z = 1$, and this reversal occurs when β crosses the value $\beta^0_{n,\mathrm{crit}}(Z=1,\mu)$. If $Z \geqslant 2$, the number density only decreases with increasing R.

3.5. Properties of the temperature distribution

The temperature may be written as

$$T(R) = T(0)\,\exp\left\{-\frac{m_i U_\parallel^2}{Z}\int_0^R \frac{\alpha_\theta^2\,dx}{[1.5+G(\beta,Z)]Tx}\right\} \times \exp\left[\frac{1+Z}{Z}\int_0^R \frac{(\ln p)'\,dx}{1.5+G(\beta,Z)}\right], \tag{63}$$

where

$$G(\beta,Z) \equiv \left(\frac{1}{2\mu}\right)^{1/2}\frac{\beta\delta}{1+Z+0.75Z\beta}. \tag{64}$$

3.5.1. High-β limit. The high-β limit is defined by the condition that $G(\beta,Z) \approx G(\infty,Z)$, which may be written as

$$\beta \gg \frac{4}{3}\frac{1+Z}{Z}. \tag{65}$$

In this limit,

$$G = \frac{4\delta}{3Z\,(2\mu)^{1/2}} \tag{66}$$

$$= 42.05 \quad \text{for } Z = 1 \quad \text{and} \quad m_i = m_p. \tag{67}$$

For the case of no flow, $Z = 1$, and $m_i = m_p$,

$$\frac{T(R)}{T(0)} = \left[\frac{n(R)}{n(0)}\right]^{1/21}. \tag{68}$$

In this case, in order for the temperature to decrease by a factor of two the density must decrease by a factor of order 10^6.

As discussed in Sec. 1.2.6 and following the energy equation (35), the high-β limit is precisely the limit in which the cancellation of the ion heat flux by the thermoelectric electron heat flux is largest.

https://doi.org/10.1017/S0022377898006928 Published online by Cambridge University Press

3.5.2. Low-β limit. The low-β limit is defined by the condition that $G(\beta, Z) \ll 1.5$, which may be written as

$$\beta \ll \frac{3}{2\delta}\frac{(1+Z)(2\mu)^{1/2}}{1-\dfrac{9Z}{8\delta}(2\mu)^{1/2}} \tag{69}$$

$$\approx \tfrac{3}{2}(1+Z)\,(2\mu)^{1/2} \tag{70}$$

$$= 0.10 \quad \text{for hydrogen.} \tag{71}$$

In this limit,

$$\left[\frac{T(R)}{T(0)}\right]^{(Z-2)/2(1+Z)} = \frac{n(R)}{n(0)}\,\exp\left(-\frac{m_i U_\parallel^2}{1+Z}\int_0^R \frac{\alpha_\theta^2\,dx}{Tx}\right). \tag{72}$$

If $Z = 2$, which includes the case of helium, the number density is constant for $U_\parallel = 0$, and increases with radius for $U_\parallel \neq 0$. If $Z > 2$, the temperature and density are correlated when $U_\parallel = 0$. If $Z = 1$, the temperature and density are anticorrelated when $U_\parallel = 0$. For the model under consideration, $U_\perp = 0$, so that if $U_\parallel = 0$ then there is no flow.

3.6. Evidence for bifurcation: double-valuedness of the total axial current for fixed outer boundary conditions

The total axial current may be written as a function of values of quantities at the cylinder radius $R = a$. One obtains

$$I_{z\pm} = \frac{caE_z\,|B_z(a)|}{2E_1(a)}\left\{-\operatorname{sign}[B_z(a)B_z{}'(a)] \pm \left(1-\frac{E_{\rm crit}^2}{E_z{}^2}\right)^{1/2}\right\}, \tag{73}$$

where $E_{\rm crit}$ is the critical electric field, defined by

$$E_{\rm crit}^2 = E_1^2(a) - \operatorname{sign}[B_z(a)B_z{}'(a)]\,E_2^2(a), \tag{74}$$

and

$$E_1(a) = \frac{c\,|B_z{}'(a)|}{2\pi\Sigma_0 T^{3/2}(a)}\frac{\Sigma_\parallel}{\Sigma_\parallel - 1}, \tag{75}$$

$$E_2(a) = \frac{c}{\Sigma_0 T^2(a)}\left[\left|\frac{B_z{}'(a)T'(a)}{B_z(a)}\right|\frac{3Zp(a)}{2\pi\,(1+Z)}\right]^{1/2}\frac{\Sigma_\parallel}{\Sigma_\parallel - 1}. \tag{76}$$

If $E_{\rm crit}^2 < 0$ then, for all values of E_z, there are two real solutions for I_z: one positive and one negative. If $E_{\rm crit} = 0$ then, for all values of E_z, there is one real, non-zero solution for I_z, and one solution with $I_z = 0$. If $E_{\rm crit}^2 > 0$ then there are no real solutions for I_z if $E_z < E_{\rm crit}$, one real solution if $E_z = E_{\rm crit}$, and two real solutions if $E_z > E_{\rm crit}$.

The solutions presented in Sec. 5 are generated by specifying boundary conditions only at $R = 0$. Once a solution is generated, the values at $R = a \equiv 50$ cm of the quantities that enter (73) are used to compute $I_{z\pm}$. One of these values must be, and is found to be, equal to the value of I_z for the solution used to compute $I_{z\pm}$. The meaning of the double-valued solution for I_z is claimed to be as follows.

It is claimed that all of the solutions to the model can be uniquely determined by specifying boundary conditions only at $R = a$, and that a subset of these boundary conditions are the quantities that enter (73) for $I_{z\pm}$. Suppose that this subset of

https://doi.org/10.1017/S0022377898006928 Published online by Cambridge University Press

boundary conditions is given. As shown in Sec. 3.1, the radial component of the Poynting flux is negative. Choosing $E_z > 0$ without loss of generality, it follows that $B_\theta(R) > 0$, so that $I_z = \frac{1}{2}cB_\theta(a)a > 0$. Then $I_z > 0$ for all solutions. If $E^2_{\rm crit} < 0$, it is claimed there is only one solution for the equilibrium state corresponding to the one positive solution to (73). If $E_{\rm crit} = 0$, it is claimed there is one solution for the equilibrium state, provided that the non-zero solution to (73) is positive. The most important case is that for which $E^2_{\rm crit} > 0$. In this case, there are no solutions for the equilibrium state when $E_z < E_{\rm crit}$. It is claimed that there is one solution for the equilibrium state when $E_z = E_{\rm crit}$, provided that the one solution to (73) is positive, and two solutions when $E_z > E_{\rm crit}$ provided that the two solutions to (73) are positive. If this is true then, when $-{\rm sign}[B_z(a)B'_z(a)]$ in (73) is positive, there are no solutions when $E_z < E_{\rm crit}$, but as E_z increases one solution comes into existence when $E_z = E_{\rm crit}$, and this solution bifurcates when E_z exceeds $E_{\rm crit}$.

Although these claims have not yet been proved for the model presented here, similar claims are proved for earlier models, as discussed in Sec. 1.2.4. In Goodman (1992, 1993) it is demonstrated that the solutions can be uniquely determined by specifying boundary conditions only at $R = a$, and numerical examples of a bifurcation of the equilibrium state are presented. Once the boundary conditions at $R = a$ are specified, the solution is generated by integrating from $R = a$ to $R = 0$. These results from earlier models, together with the existence of the double-valued expression (73), suggest that the confinement properties of a tokamak plasma can be strongly influenced by fixing conditions at the outer boundary of the plasma, and varying the applied electric field. For the bifurcations observed in Goodman (1992, 1993) the equilibrium bifurcates into a plasma-confining state as defined in Sec. 1.2.3, and a state with nearly constant temperature and pressure, and relatively small current density. This bifurcation may correspond to the L–H mode transition observed in tokamaks.

For the three solutions discussed in Sec. 5.2.1, $E^2_{\rm crit} < 0$. The values of $E^2_{\rm crit}$ for solutions (*a*), (*b*) and (*c*), are -0.0966, -2.4347×10^{-4} and $-0.0208\,{\rm V}^2\,{\rm m}^{-2}$. As already stated, since $E_z > 0$, all solutions must have $I_z > 0$. Then the positive solution for I_z obtained from (73) must equal the value of I_z computed numerically from the solution to the differential equations in Sec. 4. This requirement is a strong check on the correctness of the analytical calculations, and of the numerical procedure used to solve the differential equations. For solutions (*a*), (*b*), and (*c*), the corresponding sets of values of I_z obtained from (73) are (-1159.148, 1019.229), ($-12\,983.590$, 1535.916) and (-1796.154, 1410.449) kA. The corresponding actual values of I_z computed from the numerical solution are 1019.217, 1535.912 and 1410.433 kA, which agree closely with the positive solutions to (73), as required.

For the three solutions discussed in Sec. 5.2.2, $E^2_{\rm crit} > 0$. The values of $E_{\rm crit}$ for solutions (*a*), (*b*) and (*c*) are 0.0357, 0.0480 and $0.0520\,{\rm V\,m}^{-1}$. The corresponding values of E_z are 0.04, 0.0554 and $0.07\,{\rm V\,m}^{-1}$, so that $E_z > E_{\rm crit}$. For solutions (*a*), (*b*) and (*c*) the corresponding sets of values of I_z obtained from (73) are (10 857.334, 4104.387), (29 040.567, 9726.457), and (15 503.711, 3062.386) kA. The corresponding actual values of I_z computed from the numerical solution are 10 856.885, 9726.583 and 3062.406 kA, which agree closely with one of the solutions to (73), as required. As in the case of the first three solutions, this agreement is a strong check on the correctness of the calculations.

https://doi.org/10.1017/S0022377898006928 Published online by Cambridge University Press

4. Equations for numerical solution

The equilibrium state is determined by solving four coupled ordinary differential equations for T, p, B_z, and B_θ. These equations are

$$T' = \frac{-(1+Z)\Sigma_0(Z)T^{5/2}B_\theta E_z}{G(\beta,Z)Z\Sigma_\parallel(Z)cp}, \tag{77}$$

$$p' = \frac{m_i p\alpha_\theta^2 U_\parallel^2}{(1+Z)TR} - \left[1 + \frac{3}{2G(\beta,Z)}\right]\frac{\Sigma_0(Z)T^{3/2}B_\theta E_z}{\Sigma_\parallel(Z)c} \tag{78}$$

$$B_z' = \frac{-4\pi B_z\Sigma_0(Z)T^{3/2}B_\theta E_z}{cB^2G(\beta,Z)\Sigma_\parallel(Z)}\{G(\beta,Z)[\Sigma_\parallel(Z)-1]-1.5\}, \tag{79}$$

$$B_\theta' = \frac{-4\pi\alpha_\theta^2\Sigma_0(Z)T^{3/2}E_z}{cG(\beta,Z)\Sigma_\parallel(Z)}\{G(\beta,Z)[\Sigma_\parallel(Z)-1]-1.5\} - \frac{B_\theta}{R} + \frac{4\pi\Sigma_0(Z)E_zT^{3/2}}{c}, \tag{80}$$

subject to the constraints that

$$B_\theta(0) = 0, \tag{81}$$

$$\left(\frac{B_\theta}{R}\right)_{R=0} = \frac{2\pi\Sigma_0(Z)E_zT^{3/2}(0)}{c}, \tag{82}$$

where (82) is obtained by taking the limit of (52) as $R \to 0$. The inputs used to solve (77)–(80) are $T(0), p(0), B_z(0), U_z(0)(= U_\parallel)$ and E_z. The radius a of the cylinder must also be specified as the point at which the integration is stopped. For the solutions presented in Sec. 5 the choice $a = 50$ cm is made, since this is a reasonable value for modelling tokamak plasmas.

Hence only boundary conditions at $R = 0$ are used to generate the solutions discussed in Sec. 5. As discussed in Sec. 3.6, it is claimed that the solutions to (77)–(80) that satisfy the constraints (81) and (82) can be uniquely determined by specifying boundary conditions only at $R = a$, and that in this case one can systematically generate pairs of solutions corresponding to a bifurcation of the equilibrium state characterized by the double-valued axial current (73).

5. Numerical results

5.1. General discussion

Only a small subspace of the solution space spanned by the inputs $T(0)$, $p(0)$, $B_z(0)$, $U_z(0)$ and E_z is studied here. This subspace is chosen to cover part of the parameter range that describes fusion plasmas in tokamaks. For each of the solutions generated, profiles are presented for the temperature, pressure, number density, radial electric field, relative charge separation, β, and the axial and poloidal components of the magnetic field, velocity and current density. In addition, profiles are presented that show the contribution of the temperature-gradient-driven thermoelectric current density to the axial and poloidal current densities, and the contribution of the Hall and electron-pressure-gradient terms in Ohm's law to the radial electric field. As is shown, the thermoelectric current density can be the dominant component of the total current density, and the Hall and electron-pressure-gradient terms can

https://doi.org/10.1017/S0022377898006928 Published online by Cambridge University Press

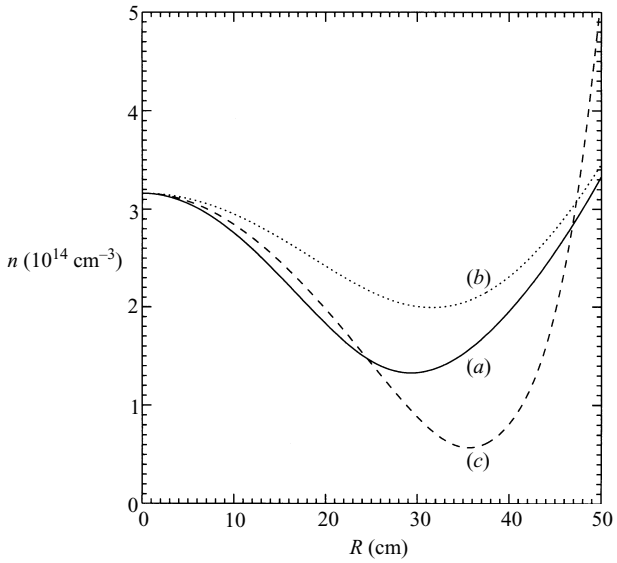


Figure 1.1. Number density versus R.

make equal or dominant contributions to the radial electric field. The plots of β are used to demonstrate that the thermoelectric component of the electron heat flux can cancel a large fraction of the proton heat flux.

Two sets of three solutions for a proton–electron plasma are presented. The temperature and density ranges of the solutions are restricted to $T \approx 8.0\,\mathrm{eV}$–$8.0\,\mathrm{keV}$ and $n \approx 10^{14}$–$10^{16}\,\mathrm{cm}^{-3}$, which includes the temperature range and the upper half of the density range of plasmas of fusion interest (Freidberg 1982). The ranges of the inputs of velocity, and electric and magnetic fields are chosen to be $0 \leqslant U_z(0) \leqslant 0.005\,c$, $0.02\,\mathrm{V\,m}^{-1} < E_z < 0.07\,\mathrm{V\,m}^{-1}$ and $1\,\mathrm{T} \leqslant B_z(0) \leqslant 3\,\mathrm{T}$. The solutions are also constrained to satisfy the conditions that $(\omega_p\tau_p)^2 \geqslant 100$, and that Λ vary by less than 50% from its value at $R = 0$ throughout the plasma. The first condition justifies the use of the high-magnetic-field limit of the transport coefficients. The second condition approximately justifies the assumption that the Coulomb logarithm is constant and equal to its value at $R = 0$.

The first set of solutions has $n \approx 10^{14}\,\mathrm{cm}^{-3}$, and are called medium-density solutions. The second set of solutions has $n \approx 10^{15}$–$10^{16}\,\mathrm{cm}^{-3}$, and are called high-density solutions. The solutions are chosen to illustrate the main properties of confined and unconfined plasmas, as defined in Sec. 1.2.3, and some of the conditions that may destroy or restore a confined state.

The radius of the cylinder is chosen to be $a = 50\,\mathrm{cm}$. All numerical calculations are done in double precision. The stepsize used to perform the radial integrations is $0.05\,\mathrm{mm}$.

5.2. Discussion of specific equilibria

5.2.1. Medium-density solutions. These solutions are shown in Figs 1.1–1.15. Solutions (*a*), (*b*) and (*c*) are labelled by solid, dotted and dashed lines. Solutions (*a*), (*b*) and (*c*) are generated using the following inputs: ($U_z(0)$, $T(0)$ (keV), $p(0)$

https://doi.org/10.1017/S0022377898006928 Published online by Cambridge University Press

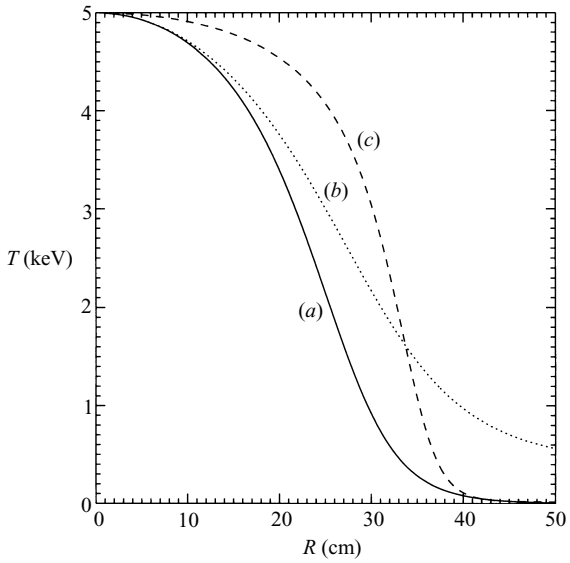


Figure 1.2. Temperature versus R. For solutions (a) and (c), $T(a) = 8.485$ and 19.057 eV.

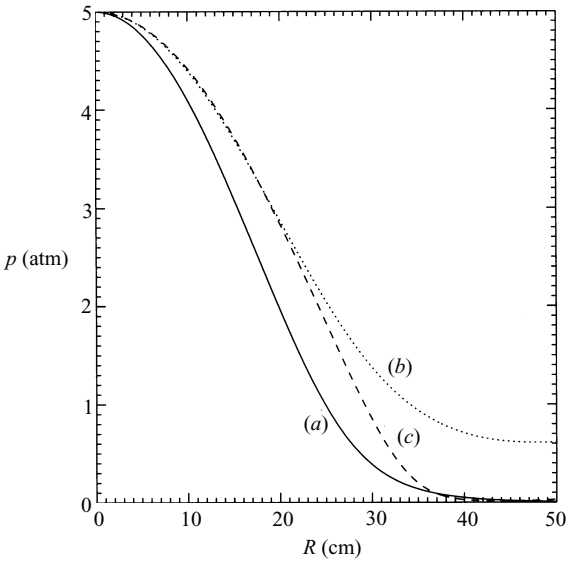


Figure 1.3. Pressure versus R. For solutions (a) and (c), $p(a) = 8.934 \times 10^{-3}$ and 3.129×10^{-2} atm.

(atm), $B_z(0)$ (T), E_z (V m^{-1})) = $(0.0, 5.0, 5.0, 1.82, 0.02)$, $(0.005\,c, 5.0, 5.0, 1.82, 0.02)$, $(0.001\,c, 5.0, 5.0, 1.0, 0.0175)$, with c in cm s^{-1}. These solutions have a density $n \approx 10^{14}$ cm^{-3}.

Solution (a) is an example of a plasma-confining state with no flow. The number density in Fig. 1.1 is a minimum at $R \equiv R_n = 29.32$ cm. According to (62), this occurs when $\beta = 0.032$. This point divides the plasma into an inner region and an outer region. The inner region of confined plasma has average values of temperature,

https://doi.org/10.1017/S0022377898006928 Published online by Cambridge University Press

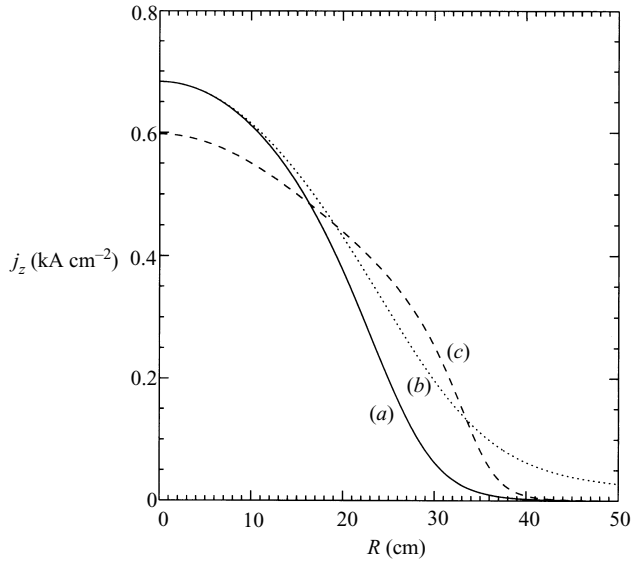


Figure 1.4. Axial current density versus R. For solutions (a) and (c), $j_z(a) = 0.217$ and $0.391\,\mathrm{A\,cm^{-2}}$.

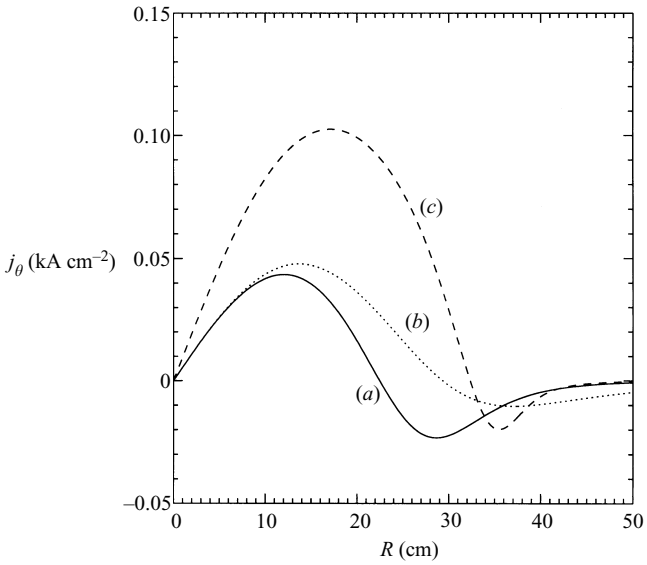


Figure 1.5. Poloidal current density versus R. For solutions (a) and (c), $j_\theta = -0.738$ and $-0.329\,\mathrm{A\,cm^{-2}}$.

pressure, and axial and poloidal current densities, shown in Figs 1.2–1.5, that are of order 10–100 times larger than in the outer region. At the outer boundary, $T(a) = 8.485\,\mathrm{eV}$, $p(a) = 8.934 \times 10^{-3}\,\mathrm{atm}$, $j_z(a) = 0.217\,\mathrm{A\,cm^{-2}}$ and $j_\theta(a) = -0.737\,\mathrm{A\,cm^{-2}}$.

Solution (b) is generated from solution (a) by increasing $U_z(0)$ from zero to $0.005\,c$. The axial and poloidal components of the flow velocity are shown in Figs 1.6 and 1.7. Since $U_z(R) = \alpha_z(R)U_z(0)$ and $U_\theta(R) = \alpha_\theta(R)U_z(0)$, the introduction of flow along the axis generates a flow parallel to **B** throughout the plasma. The rotation of

https://doi.org/10.1017/S0022377898006928 Published online by Cambridge University Press

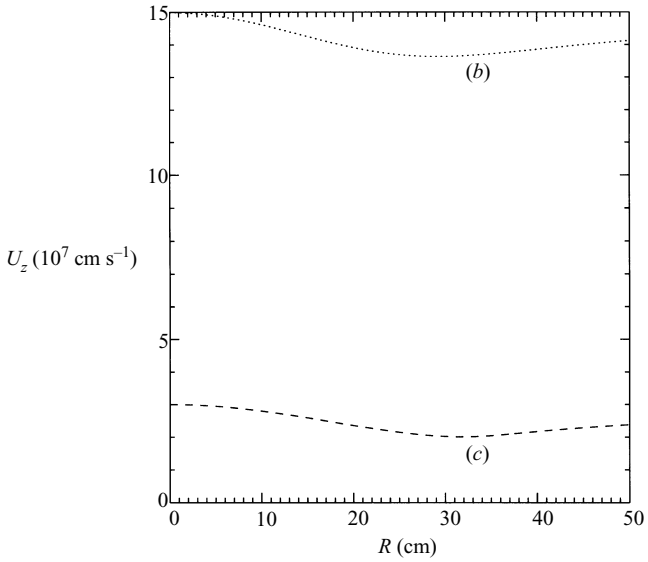


Figure 1.6. Axial flow velocity versus R.

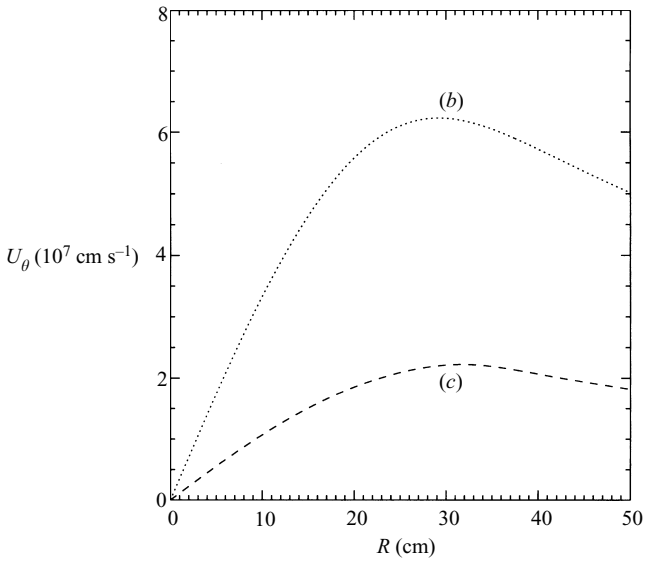


Figure 1.7. Poloidal flow velocity versus R.

the plasma generates a centrifugal force that destroys the confined state in the sense that the values of temperature, pressure, and axial and poloidal current densities at $R = a$ increase by factors of about $66, 69, 127$ and 6.4 over those of solution (a). For this solution, $R_n = 31.58\,\mathrm{cm}$.

Solution (c) is an example of a plasma-confining state with flow. It is obtained from solution (b) by decreasing the flow speed, axial magnetic field strength and driving electric field. At the outer boundary, $T(a) = 19.056\,\mathrm{eV}$, $p(a) = 3.128 \times 10^{-2}\,\mathrm{atm}$, $j_z(a) = 0.391\,\mathrm{A\,cm^{-2}}$, and $j_\theta(a) = -0.328\,\mathrm{A\,cm^{-2}}$. The restoration of a

https://doi.org/10.1017/S0022377898006928 Published online by Cambridge University Press

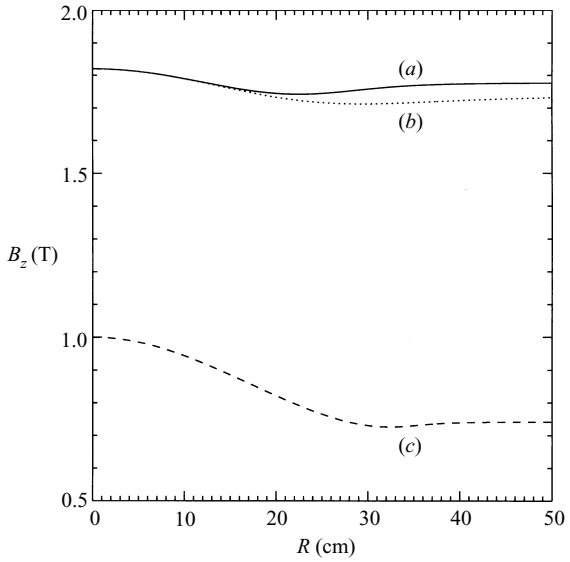


Figure 1.8. Axial magnetic field versus R.

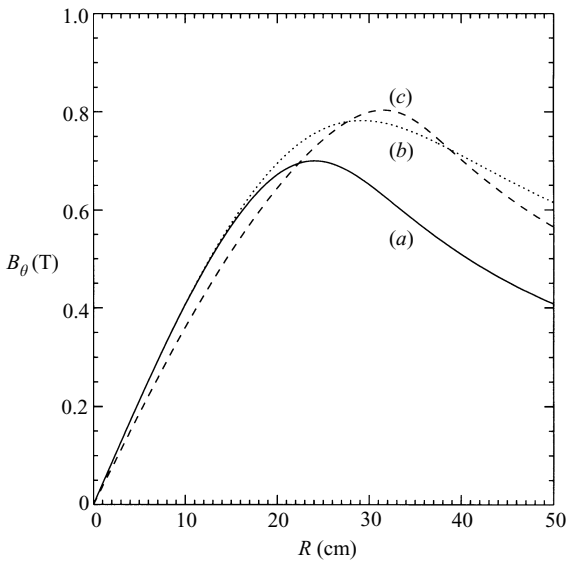


Figure 1.9. Poloidal magnetic field versus R.

plasma-confining state is due mainly to decreasing the flow speed. For this solution, $R_n = 35.62$ cm.

Solutions (a), (b) and (c) have some similar properties, which are as follows.

The axial and poloidal magnetic field components are shown in Figs 1.8 and 1.9. B_z varies slowly across the plasma, and $B_\theta \lesssim B_z$.

j_θ reverses sign before $R = R_n$, attains a minimum value near R_n, and remains negative out to $R = a$. According to (58), j_θ reverses sign when β crosses the value 0.104. Since $j_z > 0$, $\mathbf{j}$ rotates in opposite directions in the inner and outer

https://doi.org/10.1017/S0022377898006928 Published online by Cambridge University Press

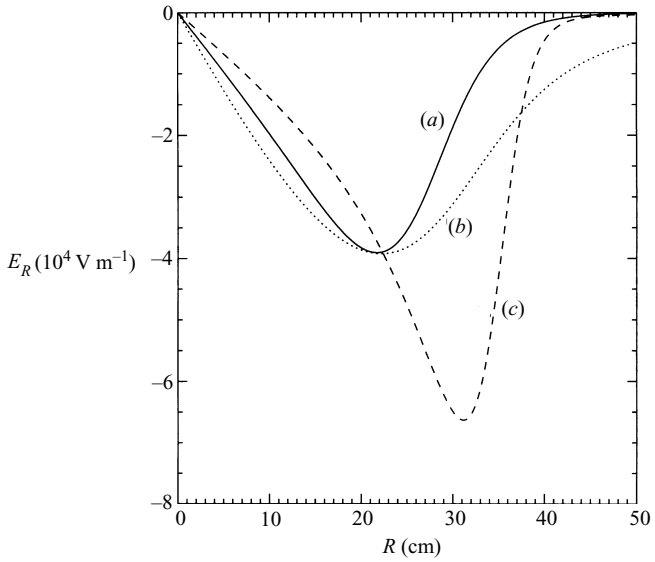


Figure 1.10. Radial electric field versus R. For solutions (a) and (c), $E_R(a) = -131.254$ and $-372.695\,\mathrm{V\,m^{-1}}$.

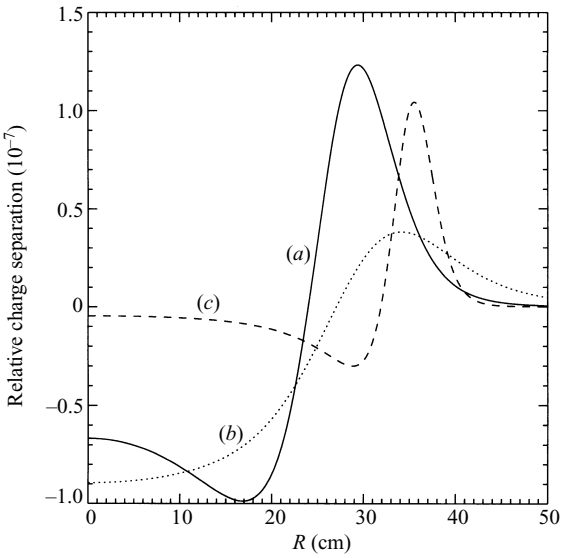


Figure 1.11. Relative charge separation $\nabla \cdot \mathbf{E}/4\pi en$ versus R. Solution (c) is multiplied by 0.1. All other profiels are unscaled. The relative charge separations at $R = a$ for solutions (a), (b) and (c) are 4.47×10^{-10}, 4.64×10^{-9} and 2.04×10^{-10}.

regions. The rate of current dissipation, given by $\mathbf{j} \cdot (\mathbf{E} + \mathbf{U} \times \mathbf{B}/c) = j_z E_z > 0$, is confined almost entirely to the region $R < R_n$. This is especially true for the plasma-confining solutions.

The radial electric field, and the related relative charge separation, given at $R = 0$ by (55), are shown in Figs 1.10 and 1.11. E_R, given by (31), is strongest at the centre of an internal electric-dipole layer, seen in Fig. 1.11 centred near $R = R_n$. The dipole

https://doi.org/10.1017/S0022377898006928 Published online by Cambridge University Press

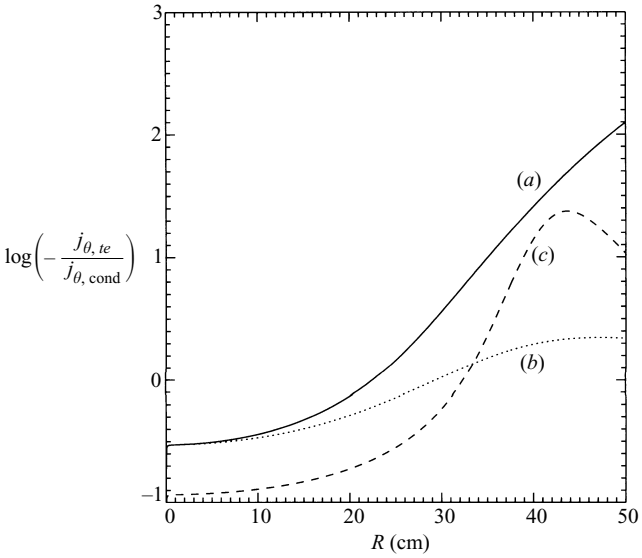


Figure 1.12. Logarithm of the ratio of the magnitude of the poloidal component of the thermoelectric current density to the poloidal component of the conduction current density versus R. The plot is chosen to start at $R = 0.01$ cm, since $j_{\theta,\mathrm{cond}}(0) = 0$.

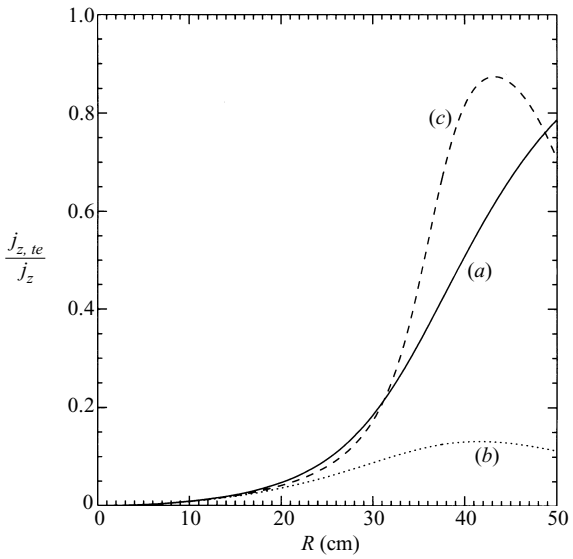


Figure 1.13. Ratio of the axial component of the thermoelectric current density to the axial component of the total current density versus R.

layer is thinnest for the plasma-confining solutions. For these solutions, the annulus centred near $R = R_n$, and several centimetres thick, is an internal boundary layer across which the charge separation, temperature, pressure and axial current density vary rapidly.

Figures 1.12 and 1.13 demonstrate the importance of the thermoelectric current density. Figure 1.12 shows that, although in the inner region ($R < R_n$) $j_\theta \approx j_{\theta,\mathrm{cond}}$,

https://doi.org/10.1017/S0022377898006928 Published online by Cambridge University Press

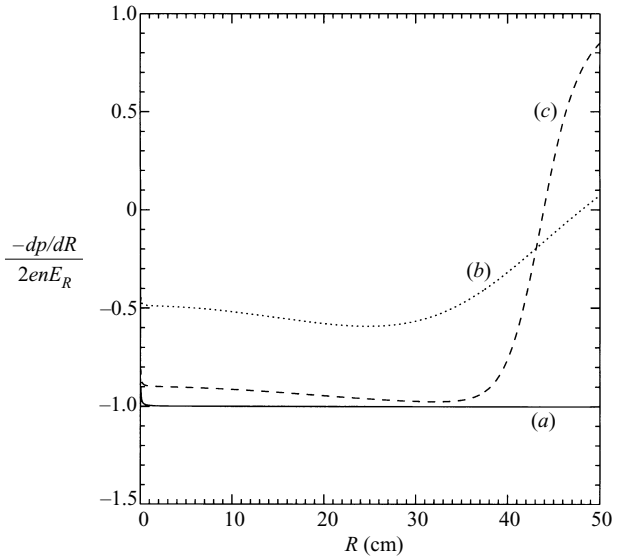


Figure 1.14. Ratio of the electric field due to the electron pressure gradient to the radial electric field versus R.

in the outer region ($R > R_n$) $j_\theta \approx j_{\theta,te}$. In the outer region $-j_{\theta,te}$ is as much as (10–100) $j_{\theta,\mathrm{cond}}$. Similarly, Fig. 1.13 shows that in the inner region $j_z \approx j_{z,\mathrm{cond}}$, but in the outer region $j_{z,te}$ can make the dominant contribution to j_z, being as much as about $6j_{z,\mathrm{cond}}$. Thermoelectric effects are rarely included in MHD modelling. The solutions presented here show that the temperature gradient-driven, thermoelectric current density can make the dominant contribution to the total current density, and so must be taken into account.

Figure 1.14 shows the relative contribution of the electron-pressure-gradient term in Ohm's law to the radial electric field. According to (32), the radial electric field may be written as

$$E_R \equiv E_{\mathrm{Hall}} + E_{p_e}, \tag{83}$$

where

$$E_{p_e} = -\frac{p'}{2en}, \tag{84}$$

using $p_e = \frac{1}{2}p$ and $n_e = n_p$. Since the Lorentz force is compressive, it follows that $E_{\mathrm{Hall}} < 0$. When $E_{p_e}/E_R \approx -1$, $E_{\mathrm{Hall}} \approx -2E_{p_e}$; when $E_{p_e}/E_R \approx 0$, $|E_{\mathrm{Hall}}| \gg |E_{p_e}|$; and when $E_{p_e}/E_R \approx 1$, $|E_{\mathrm{Hall}}| \ll |E_{p_e}|$. Solutions (*a*), (*b*) and (*c*) include all of these cases, showing that E_{Hall} and E_{p_e} can each make the major contribution to E_R. The Hall and electron-pressure-gradient terms in Ohm's law are often neglected in MHD modelling. The solutions presented here show that this omission may not be justified, especially for the case of flow parallel to the magnetic field, for which $\mathbf{U} \times \mathbf{B} = 0$, in which case there can be no cancellation between $\mathbf{E}$ and $\mathbf{U} \times \mathbf{B}/c$.

The plasma β is shown in Fig. 1.15. The discussion following the energy equation (35) indicates that, for hydrogen, if $\beta \ll 2.67$ then the heat flux is carried entirely by the ions, and is given by the familiar expression $-\kappa_\perp^i T'$. However, if $\beta \gtrsim 2.67$ then there is a significant radially inward thermoelectric electron heat flux driven by the effective electric field (25), which partially cancels the radially outward ion

https://doi.org/10.1017/S0022377898006928 Published online by Cambridge University Press

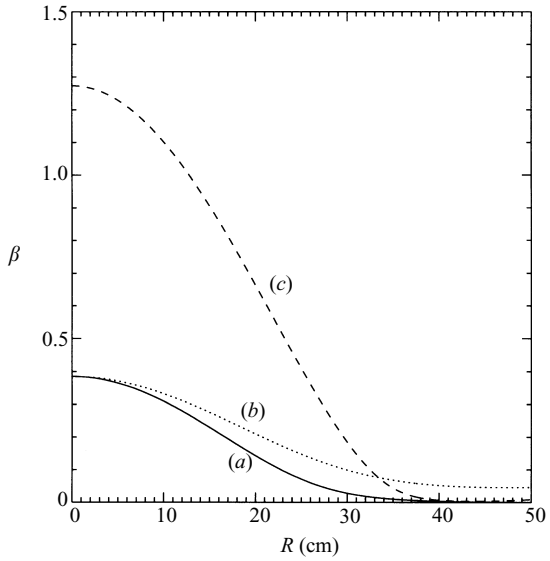


Figure 1.15. β versus R. The minimum values of β for solutions (a) and (c) are 6.85×10^{-4} and 3.98×10^{-3}.

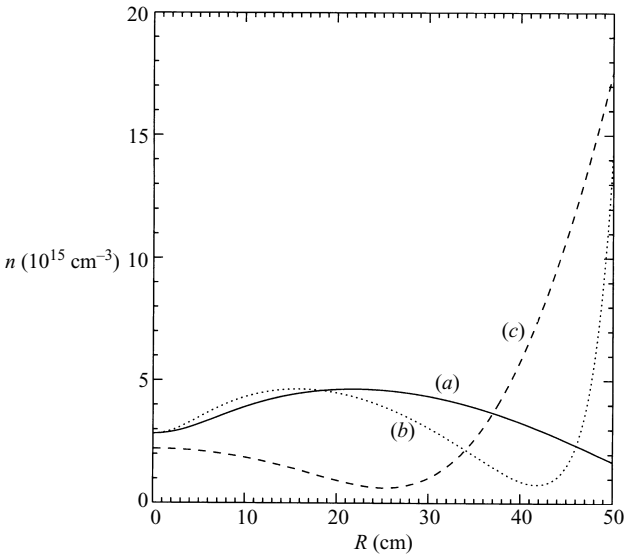


Figure 2.1. Number density versus R.

heat flux. For solutions (a), (b), and (c), the maximum values of β, which occur on the axis, correspond to a reduction in the ion heat flux by 13%, 13%, and 33%. This reduction decreases with increasing R. For the high density solutions, discussed in Sec. 5.2.2, the cancellation between the ion heat flux and the thermoelectric electron heat flux is much larger, reaching about 80%.

5.2.2. High-density solutions. These solutions are shown in Figs 2.1–2.15. Solutions (a), (b) and (c) are labelled by solid, dotted and dashed lines. Solutions (a), (b) and

https://doi.org/10.1017/S0022377898006928 Published online by Cambridge University Press

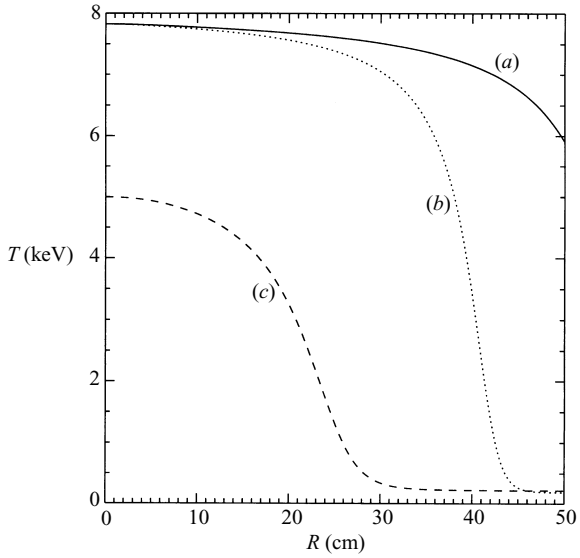


Figure 2.2. Temperature versus R.

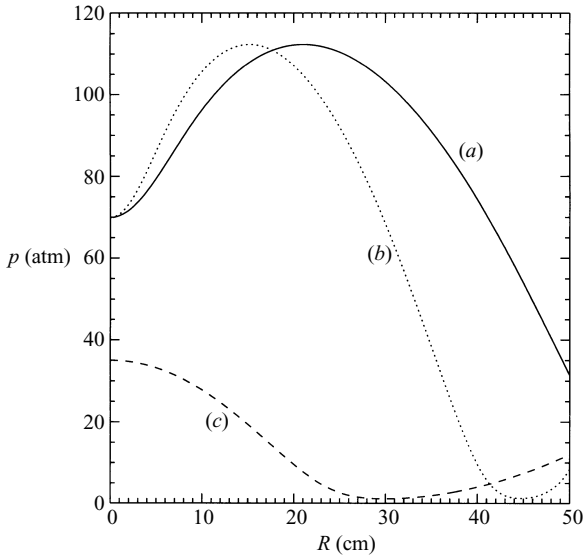


Figure 2.3. Pressure versus R.

(c) are generated using the following inputs: ($U_z(0)$, $T(0)$ (kev), $p(0)$ (atm), $B_z(0)$ (T), E_z (V m^{-1})) = (0.003 c, 7.823, 70.0, 1.0, 0.04), (0.003 c, 7.823, 70.0, 1.0, 0.0554), (0.003 c, 5.0, 35.0,3.0,0.07), with c in cm s^{-1}.

As shown by Figs 2.12–2.14, and as is the case for the medium-density solutions, the thermoelectric contribution to the current density and the contribution of the Hall and electron-pressure-gradient terms to the electric field can be large. As for the medium density solutions, the temperature gradient can drive most of the current density through thermoelectric effects. For the plasma-confining solutions (b) and (c), Figs 2.12 and 2.13 show that the thermoelectric current density

https://doi.org/10.1017/S0022377898006928 Published online by Cambridge University Press

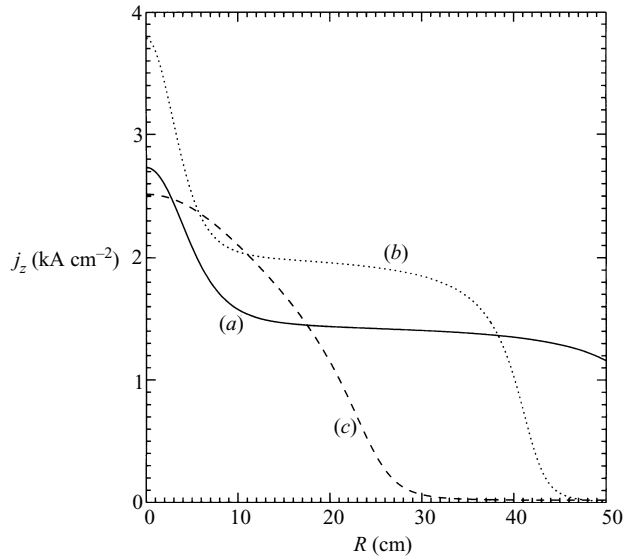


Figure 2.4. Axial current density versus R. For solutions (b) and (c), $j_z(a) = 12.145$ and $20.806\,\mathrm{A\,cm^{-2}}$.

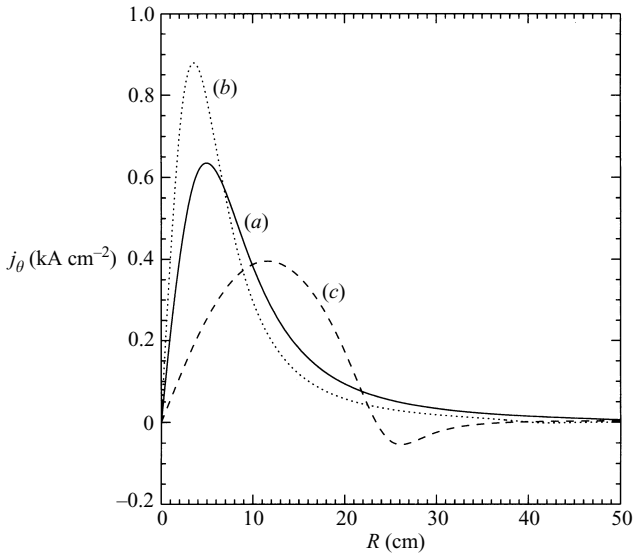


Figure 2.5. Poloidal current density versus R. For solutions (a), (b) and (c), $j_\theta(a) = 5.75$, 0.0165 and $3.397\,\mathrm{A\,cm^{-2}}$.

is strongly peaked in the internal boundary layer separating the inner region of confined plasma from the outer region of unconfined plasma. For these solutions, Fig. 2.11 shows that the relative charge separation is strongly peaked in this boundary layer, which is also an electric-dipole layer.

Solutions (a), (b) and (c) exhibit some of the properties that the medium-density solutions have in common, with the following notable exceptions.

The pressure is shown in Fig. 2.3. The momentum equation (22), and the fact

https://doi.org/10.1017/S0022377898006928 Published online by Cambridge University Press

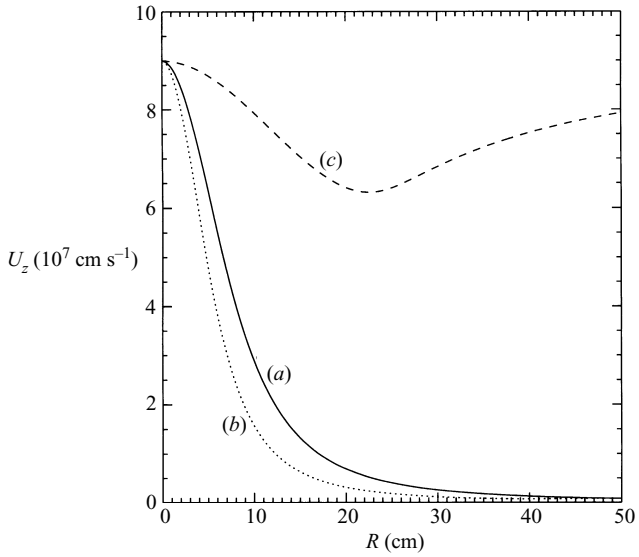


Figure 2.6. Axial flow velocity versus R.

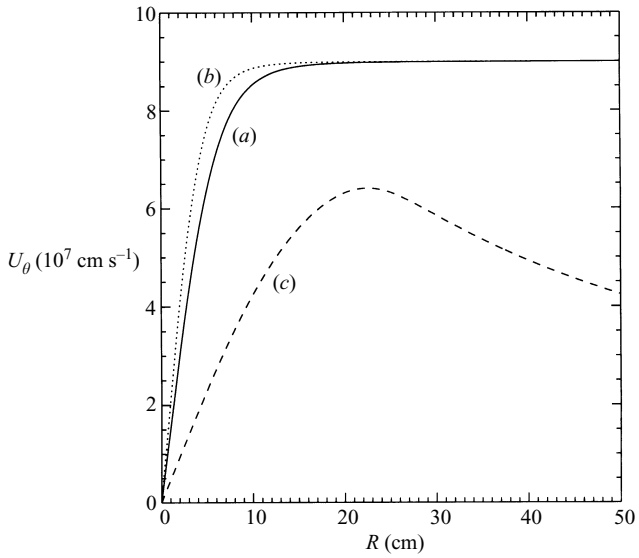


Figure 2.7. Poloidal flow velocity versus R.

that the Lorentz force is radially inward (see Sec. 3.2), imply that $p' < 0$ in the absence of flow, and suggest that $p' > 0$ for a sufficiently large value of $\rho U_\theta^2/R$. For the medium-density solutions, $p' < 0$ everywhere, and the pressure is a maximum on the axis. By contrast, the high-density solutions all exhibit intervals in which $p' > 0$. In particular, for solutions (a) and (b), the pressure is a global maximum, and the density, shown in Fig. 2.1, is a local maximum near the same point off the axis. At the point at which $p' = 0$, the Lorentz and centrifugal forces cancel exactly.

j_z is shown in Fig. 2.4. For the medium-density solutions, j_z decreases steadily with increasing R. By contrast, for the high-density solutions, j_z may exhibit a

https://doi.org/10.1017/S0022377898006928 Published online by Cambridge University Press

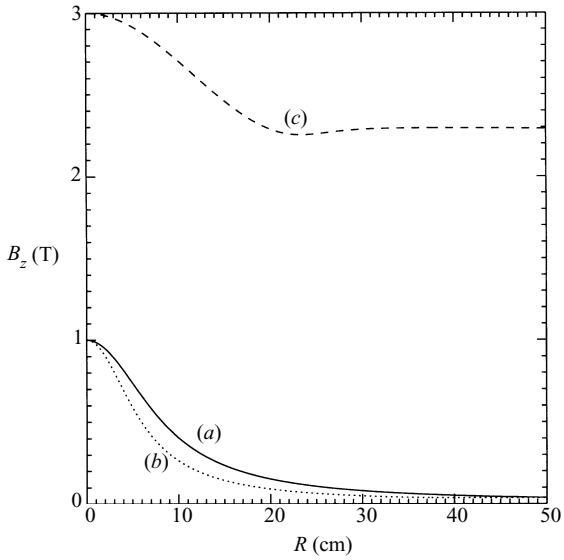


Figure 2.8. Axial magnetic field versus R.

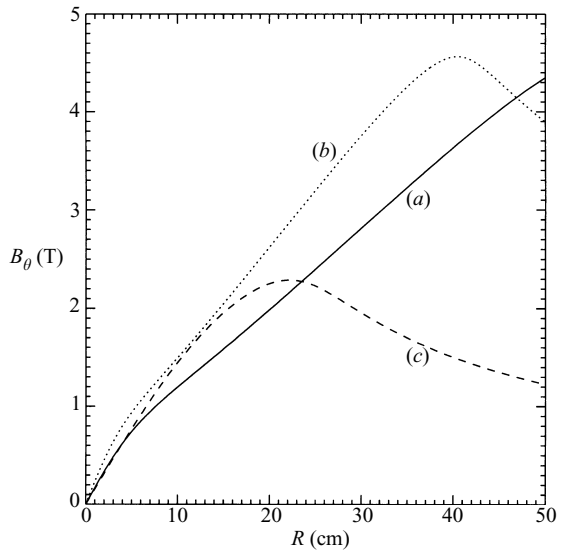


Figure 2.9. Poloidal magnetic field versus R.

plateau region of relatively high current density for both confined and unconfined solutions, as shown by solutions (a) and (b).

j_θ is shown in Fig. 2.5. For the medium-density solutions $j_\theta > (<) 0$ in the inner (outer) region. For the high-density solutions, $j_\theta > 0$ everywhere, or, as for solution (c), $j_\theta < 0$ only in the internal boundary layer that separates the inner region of confined plasma from the outer region of unconfined plasma. This boundary layer is centred near the point $R = 25.25$ cm at which the density is a minimum.

U_z is shown in Fig. 2.6. Whereas U_z varies slowly, and is almost constant for the

https://doi.org/10.1017/S0022377898006928 Published online by Cambridge University Press

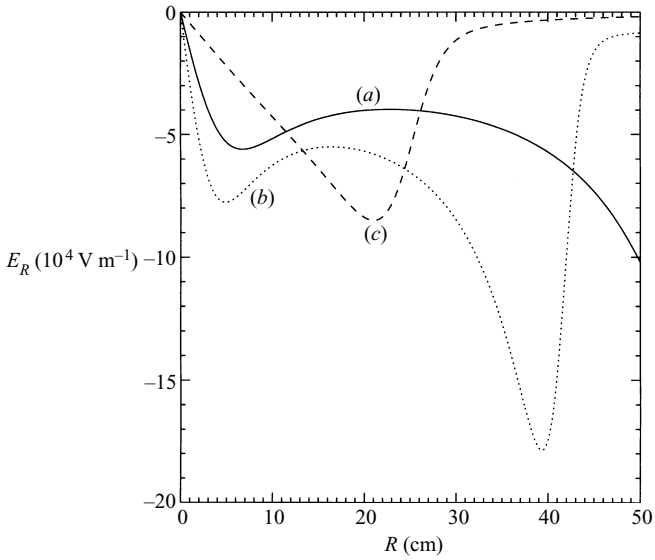


Figure 2.10. Radial electric field versus R.

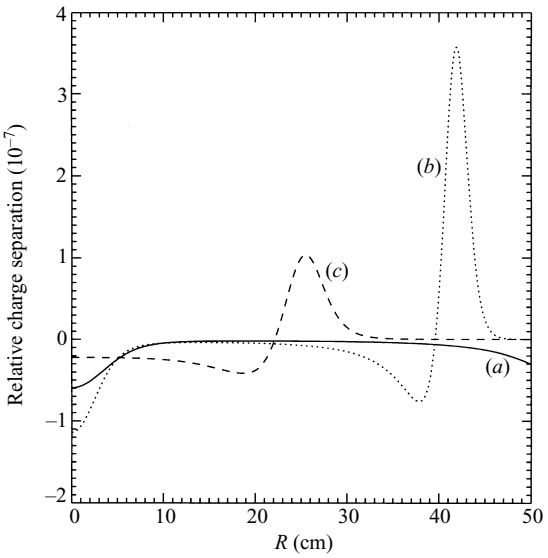


Figure 2.11. Relative charge separation $\nabla \cdot \mathbf{E}/4\pi en$ versus R. The relative charge separations at $R = a$ for solutions (b) and (c) are 2.6×10^{-11} and 1.7×10^{-11}.

medium-density solutions, for the high-density solutions it may decrease rapidly to relatively small values (of order 10^6 cm s^{-1}), as shown by solutions (a) and (b).

U_θ is shown in Fig. 2.7. Whereas U_θ increases steadily to a maximum and then steadily decreases for the medium-density solutions, U_θ increases much more rapidly for the high-density solutions, and for solutions (a) and (b) rapidly reaches a plateau about 10 cm from the axis.

B_z and B_θ are shown in Figs 2.8 and 2.9. $B_\theta \lesssim B_z$ everywhere for the medium-density solutions. By contrast, $B_\theta \gg B_z$ or $B_\theta \lesssim B_z$ in the outer region of the

https://doi.org/10.1017/S0022377898006928 Published online by Cambridge University Press

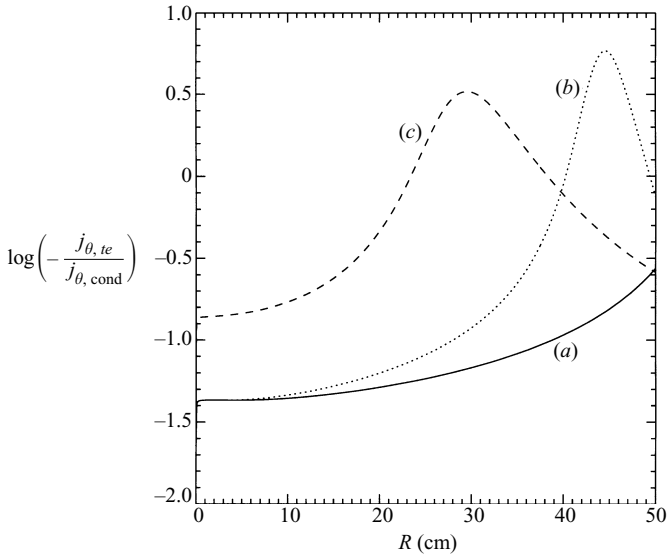


Figure 2.12. Logarithm of the ratio of the magnitude of the poloidal component of the thermoelectric current density to the poloidal component of the conduction current density versus R. The plot is chosen to start at $R = 0.01$ cm, since $j_{\theta,\mathrm{cond}}(0) = 0$.

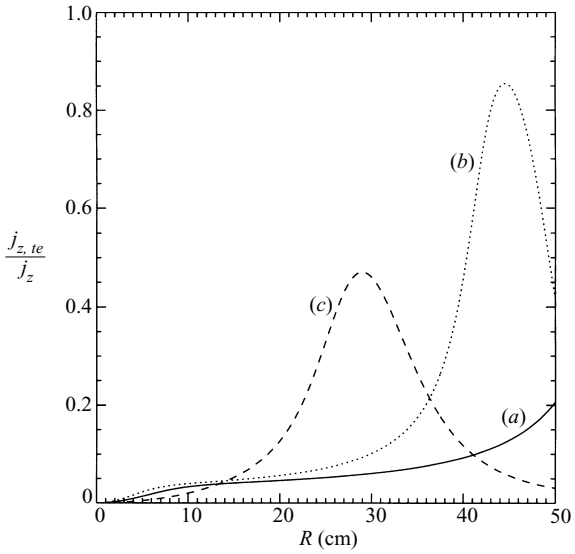


Figure 2.13. Ratio of the axial component of the thermoelectric current density to the axial component of the total current density versus R.

high-density solutions. The medium-density solutions are closest to a θ pinch, while the high-density solutions are closest to a Z pinch (Freidberg 1982).

Comparing Figs 1.12 and 2.12 shows that, although $j_{\theta,te}$ may dominate $j_{\theta,\mathrm{cond}}$ for the high density solutions, as shown by solutions (b) and (c), its contribution is generally less than it is for the medium-density solutions. For solution (a), $-j_{\theta,te}$ is always much less than $j_{\theta,\mathrm{cond}}$.

https://doi.org/10.1017/S0022377898006928 Published online by Cambridge University Press

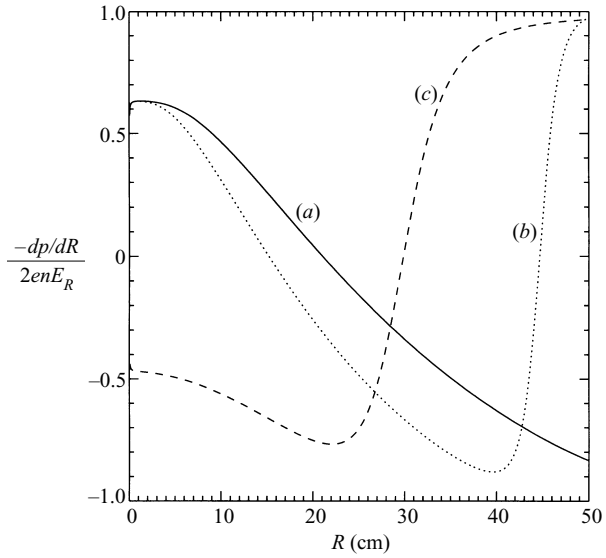


Figure 2.14. Ratio of the electric field due to the electron pressure gradient to the radial electric field versus R.

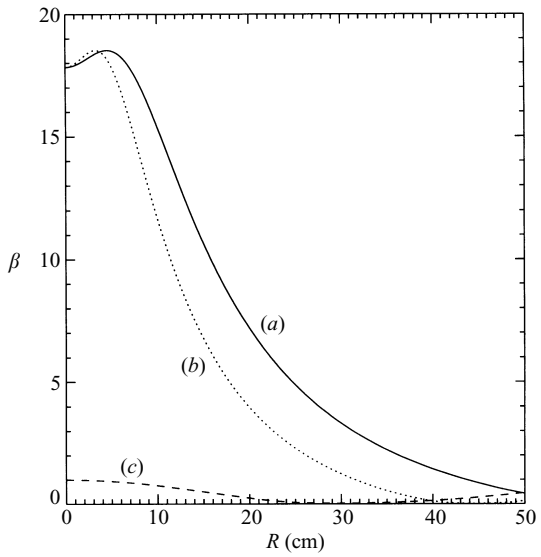


Figure 2.15. β versus R. The minimum values of β for solutions (b) and (c) are 1.69×10^{-2} and 3.07×10^{-2}.

The plots of β in Fig. 2.15 show that, near the axis, the cancellation between the thermoelectric electron heat flux and the ion heat flux leads to a reduction of the ion heat flux by 87%, 87% and 27% for solutions (a), (b) and (c). It follows from (35) that for solutions (a) and (b), the reduction in the ion heat flux exceeds 50% for $R \lesssim 33$ cm and 24 cm, respectively. Comparing the plots of β in Figs 1.15 and 2.15 with the corresponding temperature profiles in Figs 1.2 and 2.2 indicates that

https://doi.org/10.1017/S0022377898006928 Published online by Cambridge University Press

in the regions where the temperature is highest, and the temperature gradient is smallest, the thermoelectric electron heat flux is most important. As the temperature decreases, and its gradient increases, the ion heat flux grows relatively larger. In the outer region of the plasma the heat flux is carried almost entirely by the ions. This effect is especially evident for the high-density solutions (*a*) and (*b*).

6. Discussion

The MHD model presented here, which includes a realistic description of classical transport processes, provides a good indication of the importance and complexity of transport processes in the collision-dominated limit. Studying the effects of classical transport processes may also provide at least qualitative insight into the effects of collisionless transport processes, which are governed by long-range wave–particle, as opposed to short-range Coulomb, interactions.

The model exhibits a wide range of solutions that demonstrate that thermoelectric effects and the contribution to the electric field due to the electron-pressure-gradient and Hall terms in Ohm's law can be important, although these effects are usually neglected in MHD modelling of plasmas. In particular, the demonstration that temperature-gradient-driven, thermoelectric currents can make up most of the current density, and that the effective electric-field-driven, thermoelectric electron heat flux, can cancel most of the ion heat flux which is driven only by the temperature gradient, demands that thermoelectric effects be given as much importance as the more commonly considered effects due to the electrical and thermal conductivities.

The solutions to the model demonstrate the importance of anisotropic transport effects. An example of this is provided by (27) and (29), which show that the axial and poloidal components of the thermoelectric current density, which can make the dominant contributions to the current density, are proportional to $\alpha_\perp$, which is one of the off-diagonal components of the thermoelectric tensor. A second example is provided by (35), which shows that the conduction of thermal energy radially outward is proportional to $\kappa_\perp^i$, the ion thermal conductivity perpendicular to $\mathbf{B}$. A third example is provided by the thermoelectric component of the electron heat flux, which can cancel a large fraction of the ion heat flux, and which, as shown by (34), involves terms proportional to $\alpha_\perp$ and $\alpha_\perp^2$.

The energy equation (34), and the equations (26) and (28) for the current density, show that several transport coefficients may collectively determine important effects. The thermoelectric terms in (26) and (28), and the dominant thermoelectric term in (34) (i.e. the term that does not vanish in the limit $\mu^{1/2} \to 0$), are all proportional to $\alpha_\perp \sigma_\wedge / \sigma_\perp$. If thermoelectric effects or the Hall effect are neglected, this term is zero. This example emphasizes the importance of including all of the transport coefficients when developing a model.

More complex MHD models that include the effects of classical transport processes are expected to reveal the importance of other transport effects that are often neglected, in particular those due to thermoelectric effects, and the anisotropy and inhomogeneity of the tensors that describe classical transport processes. A recently developed MHD model of the solar transition region that includes the effects of classical transport (Goodman 1998) suggests that the thermoelectric and conduction current densities cancel one another over most of the region to one part in 10^4–10^5.

https://doi.org/10.1017/S0022377898006928 Published online by Cambridge University Press

This result may have important implications for proposed transition-region heating mechanisms that depend on current dissipation as a main source of thermal energy.

The critical values of β presented in Sec. 3.4 at which the poloidal current density and the gradient of the number density change sign, and the role that β plays in determining the contribution of the thermoelectric electron heat flux in the energy equation (35), emphasize the fundamental importance of this simple parameter in defining the state of the plasma. The derivation of these results shows that they implicitly contain the effects of the transport processes, providing another example of the central role that transport processes play in determining the state of the plasma. It is remarkable that the critical values of β in Sec. 3.4, and the value of β in the energy equation (35) that provides an accurate measure of the degree to which the thermoelectric electron heat flux cancels the ion heat flux, depend only on the ion charge and the electron-to-ion mass ratio. These values of β are universal in that they are the same for all solutions having the same ion charge and mass. This result suggests that real plasmas may be characterized by similar universal values of β that determine important plasma properties.

As shown in Sec. 3.6, and in earlier work (Goodman 1992, 1993), fixing boundary conditions at the outer boundary of the plasma and varying the driving electric field may cause the state of the plasma to bifurcate into a plasma-confining state and a state that does not exhibit confinement. The total axial current for the states in the bifurcation is given by (73). This bifurcation may provide a useful model for the L–H mode transition in tokamaks.

The classical transport coefficients are derived as part of a two-temperature, two-component MHD model (Balescu 1988*a*). They represent kinetic effects in a fluid model of a plasma. This model is the only tractable model of a plasma that allows the complete effects of transport to be calculated in a self-consistent way together with profiles of all of the fluid variables. The transport coefficients, which are tensors for viscosity, thermal and electrical conductivity, and thermoelectric effects, are anisotropic and may vary by many orders of magnitude throughout the plasma. Using a model of this type is the next logical step in studying the effects of transport in the MHD description beyond the frequently used approximation of using an *ad hoc*, constant, scalar resistivity and viscosity. Increases in computing speed are beginning to make such models tractable, at least in the case of one or two dimensions.

Important examples of collision-dominated plasmas that can be much better understood through the application of these models are the solar interior, photosphere, chromosphere, lower transition region, and possibly the upper transition region and lower corona. The model solutions presented in Sec. 5 may be viewed as describing the internal state of a twisted magnetic flux tube with a diameter of one metre. However, the model is valid for any diameter of the flux tube, and so may be used to study the interior of flux tubes in any fully ionized, strongly magnetized, collision-dominated region of the solar atmosphere, such as magnetic filaments with diameters of order 1 km that may exist in the lower transition region and make a major contribution to its heating (Rabin and Moore 1984).

It is of fundamental importance to be able to accurately calculate the rate at which thermal energy is generated due to dissipation, the rate at which it is conducted from one region to another, and the rate at which it is converted into elec-

https://doi.org/10.1017/S0022377898006928 Published online by Cambridge University Press

tromagnetic radiation due to atomic and molecular collisions. This calculation can only be done using a realistic description of transport processes applied in the region of parameter space that characterizes the plasma of interest. This fact stresses the importance of developing and applying such descriptions, both in the collision-dominated and in the collisionless parameter regimes.

Acknowledgements

The author thanks the referee for useful suggestions for improving the exposition of the material in the manuscript. The author thanks Steven Curtis and William Mish in the Laboratory for Extraterrestrial Physics at NASA/Goddard for support of this work. The author also thanks Stuart Jordan in the Laboratory for Astronomy and Solar Physics at Goddard for comments on the manuscript.

References

Balescu, R. 1988*a* *Transport Processes in Plasmas*, Vol. 1: *Classical Transport*. North-Holland, Amsterdam.

Balescu, R. 1988*b* *Transport Processes in Plasmas*, Vol. 2: *Neoclassical Transport*. North-Holland, Amsterdam.

Braginskii, S. I. 1965 *Reviews of Plasma Physics*, Vol. 1 (ed. M. A. Leontovich), p. 205. Consultants Bureau, New York.

Cowley, S. C. and Sudan, R. N. 1997 *Phys. Rep.* **283**, 1.

de Kluiver, H., Perepelkin, N. F. and Hirose, A. 1991 *Phys. Rep.* **199**, 281.

Dreicer, H. 1959 *Phys. Rev.* **115**, 238.

Dreicer, H. 1960 *Phys. Rev.* **117**, 329.

Freidberg, J.P. 1982 *Rev. Mod. Phys.* **54**, 801.

Galeev, A. A. and Sagdeev, R. Z. 1979 *Reviews of Plasma Physics*, Vol. 7 (ed. M. A. Leontovich), p. 257. Plenum, New York.

Goodman, M. L. 1992 *J. Plasma Phys.* **48**, 177.

Goodman, M. L. 1993 *J. Plasma Phys.* **49**, 125.

Goodman, M. L. 1998 *Astrophys. J.* **503**, 938.

Hinton, F. L. and Hazeltine, R. D. 1976 *Rev. Mod. Phys.* **48**, 239.

Hirshman, S. P. and Sigmar, D. J. 1981 *Nucl. Fusion* **21**, 1079.

Hu, P. N. 1982 *Phys. Fluids* **25**, 126.

Liewer, P. C. 1985 *Nucl. Fusion* **25**, 543.

Mihalas, D. and Mihalas, B. W. 1984 *Foundations of Radiation Hydrodynamics*, p. 49. Oxford University Press.

Parail, V. V. and Pogutse, O. P. 1986 *Reviews of Plasma Physics*, Vol. 11 (ed. M. A. Leontovich), p. 1. Consultants Bureau, New York.

Rabin, D. M. and Moore, R.L. 1984 *Astrophs. J.* **285**, 359.

Spada, M. 1992 *Proceedings of the 2nd Symposium on Plasma Dynamics: Theory and Applications, Trieste*.

Spada, M. and Wobig, H. 1992 *J. Phys. A: Math. Gen.* **25**, 1575.

Taylor, R. J., Brown, M. L., Fried, B. D., Grote, H., Liberati, J. R., Morales, G. J., Pribyl, P., Darrow, D. and Ono, M. 1989 *Phys. Rev. Lett.* **63**, 2365.

Zhang, W., Xiao, C. and Hirose, A. 1993 *Phys. Fluids* **B5**, 3961.

https://doi.org/10.1017/S0022377898006928 Published online by Cambridge University Press